Peer reviewed version

Link to published version (if available):
10.1016/j.icarus.2016.01.015

Link to publication record in Explore Bristol Research
PDF-document

University of Bristol - Explore Bristol Research
General rights

Time variability of Neptune's horizontal and vertical cloud structure revealed by VLT/SINFONI and Gemini/NIFS from 2009 to 2013

P. G. J. Irwin, L.N. Fletcher[1], D.Tice[2] and S.J. Owen[2]

Department of Physics, University of Oxford, Parks Rd, Oxford OX1 3PU, UK.

irwin@atm.ox.ac.uk

G.S. Orton

Jet Propulsion Laboratory, California Institute of Technology, 4800 Oak Grove Drive,

Pasadena, CA 91109, USA.

N.A. Teanby

School of Earth Sciences, University of Bristol, Wills Memorial Building, Queens Road,

Bristol, BS8 1RJ, UK

and

G.R. Davis

Square Kilometre Array Organisation, Jodrell Bank Observatory, Lower Withington

Macclesfield, Cheshire, SK11 9DL, UK

---

[1]Now moved to Department of Physics and Astronomy, University of Leicester, University Road, Leicester, LE1 7RH, UK

[2]No longer in planetary research.

ABSTRACT

New observations of Neptune's clouds in the near infrared were acquired in October 2013 with SINFONI on ESO's Very Large Telescope (VLT) in Chile. SINFONI is an Integral Field Unit spectrometer returning a 64×64 pixel image with 2048 wavelengths. Image cubes in the J-band (1.09 – 1.41 μm) and H-band (1.43 – 1.87 μm) were obtained at spatial resolutions of $0.1''$ and $0.025''$ per pixel, while SINFONI's adaptive optics provided an effective resolution of approximately $0.1''$. Image cubes were obtained at the start and end of three successive nights to monitor the temporal development of discrete clouds both at short timescales (i.e. during a single night) as well as over the longer period of the three-day observing run. These observations were compared with similar H-band observations obtained in September 2009 with the NIFS Integral Field Unit spectrometer on the Gemini-North telescope in Hawaii, previously reported by Irwin et al., Icarus 216, 141-158, 2011, and previously unreported Gemini/NIFS observations at lower spatial resolution made in 2011.

We find both similarities and differences between these observations, spaced over four years. The same overall cloud structure is seen with high, bright clouds visible at mid-latitudes ($30 – 40°$N,S), with slightly lower clouds observed at lower latitudes, together with small discrete clouds seen circling the pole at a latitude of approximately $60°$S. However, while discrete clouds were visible at this latitude at both the main cloud deck level (at 2–3 bars) and in the upper troposphere (100–500mb) in 2009, no distinct deep (2–3 bar), discrete circumpolar clouds were visible in 2013, although some deep clouds were seen at the southern edge of the main cloud belt at 30–40°S, which have not been observed before. The nature of the deep sub-polar discrete clouds observed in 2009 is intriguing. While it is possible that in 2013 these deeper clouds were masked by faster moving, overlying

features, we consider that it is unlikely that this should have happened in 2013, but not in 2009 when the upper-cloud activity was generally similar. Meanwhile, the deep clouds seen at the southern edge of the main cloud belt at 30 – 40°S in 2013, should also have been detectable in 2009, but were not seen. Hence, these observations may have detected a real temporal variation in the occurrence of Neptune's deep clouds, pointing to underlying variability in the convective activity at the pressure of the main cloud deck at 2–3 bars near Neptune's south pole and also in the main observable cloud belt at 30 – 40°S.

Subject headings: planets and satellites: atmospheres — planets and satellites: individual (Neptune)

1. Introduction

The highly dynamic clouds of Neptune have long fascinated planetary astronomers since Voyager 2's flyby of that planet in 1989. Since that time, with the advent of techniques such as Adaptive Optics operating with larger and larger telescopes, ground-based observations of this most distant of the planets have improved beyond all recognition and the atmosphere of Neptune has been discovered to be even more active and dynamic than that seen by Voyager 2. In addition to larger telescopes and better imaging, a new class of instruments, Integral Field Unit (IFU) spectrometers, have been constructed, such as the NIFS instrument on Gemini-North and the SINFONI instrument at the European Southern Observatory's (ESO) Very Large Telescope (VLT), which simultaneously map the entire FOV of the instrument at thousands of wavelengths with spectral resolving powers in excess of $R = \lambda/\Delta\lambda = 1000$.

Gemini/NIFS observations of Neptune recorded in the H-band in 2009 ($1.48 - 1.80 \ \mu$m) were presented by Irwin et al. (2011) and used to determine the vertical cloud structure of particular features at several locations on Neptune's disc over a period of several days. High clouds were seen at mid latitudes (30–40°N,S) (with tops reaching to and in some cases above the expected tropopause level), slightly lower clouds observed at more equatorial latitudes near the morning terminator, and discrete clouds detected around the south pole at $\sim 60°$S. These sub-polar clouds were seen to be of two types: one with very high cloud tops (extending to the tropopause again), and another which were apparently confined to the level of the main cloud deck at 2–3 bars. Since clouds at these two levels move with different wind speeds due to vertical wind shear, the upper clouds occasionally obscured the lower ones and so it was not possible to determine categorically whether the deeper clouds were long-lived or transient. It is possible that one of the deep clouds was present throughout the seven-day observing run, but one of the features seems to have appeared

and disappeared during a few days, which is remarkably fast for feature changes at the main cloud deck level and would indicate vigorous convective activity.

Observing Neptune from the Earth is complicated by the fact that its rotational period of 16.11 hours, as determined by the Voyager 2 Radio Science Experiment (e.g. Lacacheux et al. (1993)), means that the hemisphere of Neptune observed on one night is almost exactly the opposite to that which was observed on the previous night, and so we have to wait two nights to see the same feature at the same place on Neptune's disc. During this long period the cloud features are distorted by Neptune's zonal winds, which are extremely strong and change enormously with latitude leading to huge latitudinal wind shears that can tear apart newly formed cloud features on timescales of a few hours. To quantify this level of shear, the winds at the equator are strongly retrograde (–400 m/s, Sromovsky et al. (1993)) and thus the effective rotation period is 18.8 hours, while in the sub-polar jets the effective rotation period is as small as 11 hours.

To counter these observational problems and also determine how Neptune's cloud activity is evolving, we proposed to use the SINFONI instrument on VLT in 2013 to observe Neptune again, but this time making two observations per night, one near the beginning of Neptune's transit and one near the end so that we could observe the same cloud features over a few hours as they transited the disc. The goals of our observations were to: 1) determine how quickly Neptune's cloud features evolve with time; 2) determine if the equatorial clouds seen near Neptune's morning terminator in 2009 survive as they pass across Neptune's disc; and 3) determine the spatial distribution of deep discrete cloud features and monitor any changes that may have occurred since 2009.

2. VLT/SINFONI Observations

Observations of Neptune were made with the SINFONI instrument in October 2013 at the European Southern Observatory (ESO) Very Large Telescope (VLT) in La Paranal, Chile. At the time of observation, the diameter of Neptune's disc was $2.3''$, while the sub-observer latitude was $27.73°$S. SINFONI is an Integral Field Spectrograph that can make use of Adaptive Optics to yield a spatial resolution of typically $0.1''$. Each one of SINFONI's 32 slitlets is imaged onto 64 pixels of the detector, giving 64×32 individual spectra, each with 2048 wavelengths, which are usually doubled in the cross-slit direction to give 64×64 pixel 'cubes'. SINFONI has three pixel scale settings: $0.25''$, $0.1''$ and $0.025''$ giving Fields of View (FOV) of $8'' \times 8''$, $3'' \times 3''$ and $0.8'' \times 0.8''$, respectively. Neptune was observed on three nights from October 9th to 12th 2013 (UT) using the H- and J-grisms, which have spectral resolutions of $R = \lambda/\Delta\lambda \sim 2000$ and 3000, respectively. The individual observations are listed in Table 1. Since the disc size of Neptune comfortably fits in the FOV for the $0.1''$ plate scale, this was the default mode of operation. However, to increase the spatial resolution, observations were also made on the second and third nights with the $0.025''$ plate scale and stepping the FOV across the planet's disc, building up 4×4 mosaics.

The data were reduced with the ESO VLT SINFONI pipeline, but correction for (i.e. removal of) the stellar absorption features of the telluric standard star was made using the Spextool (Cushing et al. 2004) *xtellcor-general* package, which uses the method of Vacca et al. (2003). Photometric correction was achieved by integrating the observations of the standard (A0V) star (HIP110963) across the entire FOV, using the quoted 2MASS (Cutri et al. 2003) J- and H-magnitudes of 8.603 and 8.601 and the 2MASS J- and H-filter profiles respectively. Geometric registration was done by visually aligning the images against a Neptune reference wire-grid, which was then used for determining the latitude, longitude, and emission angles; planetocentric latitudes were assumed throughout. We also

corrected for the airmass difference between each observed planet frame and the standard star reference.

Figure 1 shows a typical reflectance spectrum of Neptune as measured by IRTF/SpeX[1], together with the pressure level at which the two-way transmission to space is 0.5 for cloud-free conditions, assuming the standard atmospheric profile described in the next section. The main absorption features seen in Neptune's near-IR spectrum are formed by gaseous methane. At wavelengths of strong methane absorption sunlight cannot penetrate very far, and thus any light we see must have been reflected from hazes in the stratosphere. Conversely in regions of weak absorption sunlight can penetrate to be reflected from clouds at the deepest levels. Hence, such spectra allow us to probe the cloud density over a wide pressure range. In this paper, we present many false colour plots that show the distribution of deep, intermediate-level and high clouds/hazes. To map the deepest clouds we only use wavelengths where the two-way transmission to space exceeds 0.5 at the 3-bar level. We shall call this the 'F3.0' filter. To map the intermediate-level clouds we choose only those wavelengths where the two-way transmission to space is **less** than 0.5 at the 1.25 bar level ('F1.25' filter), and to map the highest clouds/hazes we choose only those wavelengths where the two-way transmission to space is less than 0.5 at the 0.2 bar level ('F0.2' filter). The wavelengths covered by these three 'filters' in the 0.9 – 1.87 μm range are shown in Fig. 1. The mosaicked H-band appearance of Neptune recorded from 00:30 – 01:25UT (observation 'OB36') on October 12th 2013, using the 0.025″pixel scale in these three 'filters' is shown in the top row of Fig.2, while the appearance recorded slightly earlier (00:01 – 00:03UT, observation 'OB34') at the lower 0.1″pixel resolution is shown in Fig. 3. The bottom rows of Figs.2 and 3 show scaled differences between these images, highlighting the cloud density at low and medium altitudes (the 'F0.2' map (panel (c)) already shows the

---

[1]http://irtfweb.ifa.hawaii.edu/ spex/IRTF_Spectral_Library/

cloud/haze density at high altitudes), and also shows the aspect of Neptune at the time of observation. Figure 4 shows false-colour representations of all the useable H-grism and J-grism data recorded in 2013, with red used to indicate the deep clouds ('F3.0'), green for the intermediate-level clouds ('F1.25'), and blue for the highest clouds ('F0.2'). As can be seen, J- and H-band observations were taken at similar times and provide complementary coverage, although it is apparent that the J-band observations are more affected by upper tropospheric and stratospheric hazes, making them appear more yellowish in the false-colour scheme chosen. This is understandable given their shorter wavelength (1.3 μm compared with 1.6 μm) and the small estimated size of such haze particles ($\sim 0.1 - 1\mu$m), which leads to their cross-sectional area diminishing rapidly with increasing wavelength. Since Neptune rotates so rapidly and latitudinal wind shear distorts clouds so quickly, it is difficult to compare the raw images in Fig. 4, recorded over several days, with each other. To make this easier, we have plotted the highest quality H-band observations (which are less affected by haze and atmospheric seeing and thus clearer than the J-grism images) on a grid in Fig.5, where the x-position is determined from the central meridian longitude at the time of observation, while the y-position is the digital date (i.e. 00:00 on October 10th is 10.0, 06:00 on October 10th is 10.25, etc.). This plot allows us to compare observations taken with notionally the same 'face' of Neptune pointed towards Earth and also to see the temporal (if any) development of clouds as they traverse across the face of the planet. The 'face' of Neptune seen from the Earth can be understood more clearly in Fig.6, which shows how Neptune's appearance would change on the time versus central meridian longitude grid of Fig.5 if it were totally cloudy on one side and cloud-free on the other for two cases: 1) where the rotation period is 16.11 hrs at all latitudes; and 2) where the rotation period varies with latitude resulting from the zonal wind profile of Sromovsky et al. (1993). In the second case, which is the real case on Neptune, it can be seen that the differential rotation quickly leads to significant distortion of the the white 'face'. We could have tried to ameliorate the

effects of this using 'snakeskin' plots (i.e. where the image is mapped on to a rectangular latitude/longitude cylindrical projection) and applying latitudinally dependent corrections, but Fig.6 makes it clear that such plots would themselves become quickly distorted and hard to decipher. In addition, our spatial resolution is not sufficiently good for most of our observations to produce accurate cylindrical (or 'snakeskin') maps, especially near the South Pole. Hence, we settled on the method shown in Fig.5 of displaying our unreprojected observations on a time versus central meridian longitude grid, which shows our observations in their least processed form and gives some indication of which 'face' of Neptune is being observed, although the latitudinally dependent distortions highlighted by Fig.6 must be borne in mind.

2.1. Observations of near-equatorial intermediate-level clouds and comparison with Gemini/NIFS (2009)

It can be seen that these VLT observations provide excellent coverage of Neptune's cloud structure, especially the 4×4 mosaicked observations taken with the $0.025''$plate scale, which show excellent spatial resolution. The $0.025''$observations on the 2nd night unfortunately had the frame rotated with respect to the sample grid direction, leading to small gaps between the 'tiles', but this error was recognised and corrected for the 3rd night of observations. We can see considerable temporal development of the clouds. Observations on the 1st and 3rd nights were taken with similar central-meridian longitudes, assuming a 16.11-hr rotation rate (as can be seen in Fig.5). Some similarities can be seen, including the presence of a bright white cloud near Neptune's south pole, which does not seem to have evolved greatly over the elapsed 2 days. At equatorial and mid-latitudes, yellowish clouds are visible in the false-colour plots, which are intermediate-level clouds that are visible in the red (F3.0) and green channels (F1.25), but not so high as to be visible in the blue

channel (F0.2). Here we can see clear latitudinal wind shear in Neptune's atmosphere as the best correspondence between the 1st and 3rd nights is between the first image recorded on the 1st night and the last image recorded on the 3rd night. Since the winds are strongly retrograde at equatorial latitudes, the rotation period is effectively greater and so it takes longer for the same clouds to appear in the central meridian, as can be seen here. However, Fig.6 shows that small errors in the differential rotation rate can lead to large errors in the observed East-West position of a feature, even after just a couple of days. Assuming that the intermediate-level cloud features seen on the 3rd night are indeed the same as those seen on the 1st night (which they appear to be given Neptune's assumed latitudinal wind profile), however, we can conclude these intermediate-level clouds survive for at least a couple of rotations of the planet. In Gemini/NIFS observations of Neptune made in 2009, Irwin et al. (2011) found that such clouds were only seen near the morning terminator. However, there were not enough clouds or sufficiently well time-resolved observations to determine if these clouds were simply local-time induced features or whether they were longer lived and survived their transit across Neptune's visible disc. This can be seen in Fig.7, which shows the 2009 Gemini observations in the same format as in Fig.5, plotted as a function of time versus central meridian longitude. Here we can see that observations were well spaced over central meridian longitude, with little overlap, except after the passage of 5-6 days during which time wind shear and general evolution have distorted the clouds so much as to make them unrecognisable. The new VLT/SINFONI observations unequivocally confirm that these equatorial intermediate-level clouds are not ephemeral and last for several days.

2.2. Observations of south sub-polar deep clouds and comparison with Gemini/NIFS (2009 and 2011)

One of the most interesting features of the 2009 Gemini/NIFS observing campaign was the presence of deep clouds near Neptune's south pole (Irwin et al. 2011). In the Gemini/NIFS observations made on 1st, 5th and 6th September 2009 (Fig.7), we can see discrete red-coloured clouds near the south pole. The clouds are coloured red because they can only be seen at continuum wavelengths where the absorption of methane is least and must thus reside at pressures > 1.25 bar, presumably at the main cloud deck level, estimated to lie at around the 2–3 bar level. Irwin et al. (2011) showed that at least one of these clouds was long-lived, but was occasionally obscured by overhead clouds lying at levels of different wind speed. The new 2013 VLT/SINFONI observations show no evidence of such deep sub-polar clouds. However, several such clouds can be seen at the southern edge of the bright cloud belt at 30–40°S (most clearly seen in rows 4-6 of Fig.4), where they were not apparent in 2009. Later Gemini/NIFS observations of Neptune, previously unpublished, were also recorded on several nights between 30th August and 11th September 2011 (Table 2). During this apparition, the Adaptive Optics module was non-functional and so spatial resolution was limited to the atmospheric seeing. Hence, these observations are much less spatially resolved than the 2009, and now 2013 observations. However, they were made with the I, J and H grisms and thus have greater spectral coverage. Fig.8 shows these 2011 observations in the same format as in Figs. 5 and 7, plotted as a function of time versus central meridian longitude; the grism used is indicated by each image. In this plot we can see that the images become progressively more 'yellow' as we move from H- ($1.47 - 1.80 \ \mu$m), through J- ($1.14 - 1.36 \ \mu$m) to the I-grism ($0.94 - 1.16 \ \mu$m), indicating rapidly increasing optical depth of tropospheric/stratospheric hazes as we move to shorter wavelengths. Although of poorer spatial resolution, a discrete deep sub-polar cloud as was seen in 2009 should have been discernible in 2011, but such features are absent as they

²¹⁵ were also absent in the 2013 observations reported here. The fact that no such features are
²¹⁶ apparent after 2009 suggests that such clouds may be short-lived.

²¹⁷ ## 3.   Radiative Transfer and Retrieval Analysis

²¹⁸ To quantitatively analyse the new VLT/SINFONI H-band spectra, they were first
²¹⁹ smoothed to a lower spectral resolution using a a triangular-shaped instrument function with
²²⁰ Full Width Half Maximum (FWHM) = 0.002μm to simulate the IRTF-SpeX instrument,
²²¹ giving a spectral resolution of $R \sim 775$. Although this sacrificed spectral resolution, it
²²² greatly increased our computation speeds and improved the signal-to-noise (SNR) ratio.
²²³ This choice was justified by our previous high spectral resolution analysis of Neptune
²²⁴ spectra (Irwin et al.   2014). From this analysis we concluded that, for cloud parameter
²²⁵ retrievals, the lower IRTF-SpeX resolution was the best compromise between computational
²²⁶ efficiency, vertical resolution and SNR. Smoothing the spectra further would lower the noise
²²⁷ levels (i.e. increase the SNR), but degrade the vertical resolution, while a higher spectral
²²⁸ resolution greatly increases the computation time of the radiative transfer code (which uses
²²⁹ a Matrix-Operator multiple scattering model), while not greatly increasing the vertical
²³⁰ resolution due to the lower SNR.

²³¹ ### 3.1.   Temperature/Abundance Profiles

²³² The temperature and abundance profile assumed in this study was the same as
²³³ that used by Irwin et al.   (2014). The temperature profile was based on the 'N' profile
²³⁴ determined by radio-occultation from Voyager 2 by Lindal (1992) and the He/H_2 ratio was
²³⁵ set to 0.177, which leads to a helium volume mixing ratio of 0.15 at altitudes of negligible
²³⁶ methane abundance, assuming 0.3% nitrogen, as favoured by Conrath et al.   (1993) and

Burgdorf et al. (2003). Note that apart from at the south pole, Fletcher et al. (2014) found very little temporal evolution of Neptune's temperature structure from the Voyager epoch to more recent times near the southern summer solstice, so using the Lindal (1992) profile is reasonable. The methane abundance profile was set with a deep CH_4 mole fraction of 4% and the volume mixing ratio limited to a maximum relative humidity of 60%, as recommended by Karkoschka and Tomasko (2011), but the stratospheric abundance was set to $(1.5 \pm 0.2) \times 10^{-3}$ as recommended by Lellouch et al. (2010). Although Karkoschka and Tomasko (2011) find that the deep abundance of CH_4 reduces at high southern latitudes, our analysis here is limited to latitudes where the assumption of latitude-invariance is a reasonable approximation.

3.2. Gaseous Absorption data and Scattering Radiative Transfer Model

These data were analyzed with the WKMC-80K line database (Campargue et al. 2012) in the same method as described by Irwin et al. (2014). The spectra were fitted with the NEMESIS (Irwin et al. 2008) radiative transfer and retrieval code, using a correlated-k model (Lacis and Oinas 1991) and methane k-tables derived from the WKMC-80K line data, assuming the IRTF-SpeX triangular instrument function with FWHM = 0.002 μm. These k-tables were computed using the hydrogen-broadened methane line shape of Hartmann et al. (2002) (suitable for atmospheres where H_2 is the main constituent) and have a line wing cut-off of 350 cm^{-1}, which we previously found to give good fits to our Uranus and Neptune Gemini/NIFS observations. Since the atmospheric composition and temperature of Uranus and Neptune are very similar in the upper troposphere/lower stratosphere it is reasonable to expect the methane lines of Neptune to be broadened in the same way as for Uranus. For this k-table, a CH_3D/CH_4 ratio of 3.6×10^{-4} determined from Uranus by de Bergh et al. (1986) was assumed. Although Irwin et al. (2014)

revised this value for Neptune downwards to 3.0×10^{-4}, the effect on cloud retrievals at IRTF/SpeX resolution is not significant and so there was no need to recompute the table. For $H_2 - H_2$ and $H_2 - He$ collision-induced absorption (CIA) we used the coefficients of Borysow (1991, 1992) and Zheng and Borysow (1995) and an equilibrium ortho/para-H_2 ratio was assumed at all altitudes and latitudes, consistent with the latitudinal mean of results from the Voyager IRIS experiment at the tropopause or higher pressures (Conrath et al. 1998), although the effect of the para-H_2 fraction on the spectra in this wavelength band is insignificant. In addition to $H_2 - H_2$ and $H_2 - He$ CIA, $H_2 - CH_4$ and $CH_4 - CH_4$ collision-induced absorption was also included (Borysow and Frommhold 1986, 1987). The spectra were simulated using a Matrix Operator multiple scattering code, based on the method of Plass et al. (1973), including the Rayleigh scattering by the air molecules themselves, with 5 zenith angles (with Gauss-Lobatto calculated ordinates and weights) and N Fourier components to cover the azimuth variation, where N is set adaptively from the viewing zenith angle, θ, as $N = \mathrm{int}(\theta/3)$. To perform this calculation the reference temperature, pressure and abundance profiles were split into 39 levels equally spaced in log pressure between 6.5 bar and 0.001 bar. The reference solar spectrum of Fiorenza and Formisano (2005) was used to simulate the solar flux.

3.3. Cloud Models

When modelling the 2009 Gemini/NIFS H-band observations, Irwin et al. (2011) favoured a simple two-cloud model, with a cloud in the 2–3 bar region, which we shall henceforth call the 'Tropospheric Cloud', and a second cloud near the tropopause at 0.1 bar. At most locations the opacity of this second cloud was found to be very low and its low pressure suggests it is some form of haze. However, in Neptune's mid-latitude cloudy zones at 30–40°N,S, the opacity of this 'Haze' becomes so large and spatially structured

that it more closely resembles a second, low-pressure condensation cloud, for which the existing haze particles act as condensation nuclei. However, for ease of identification we shall henceforth call this layer the 'Haze'. Using the then best-available methane absorption data of Karkoschka and Tomasko (2010), Irwin et al. (2011) achieved a reasonably close fit by setting the extinction cross-section spectra of the particles in both layers to be as that calculated with Mie theory assuming a complex refractive index of $1.4 + 0i$ (with a standard Gamma distribution of sizes with mean radius 1.0 μm and variance 0.05), but adjusting the single scattering albedo manually, favouring, from limb-darkening considerations, a value of 0.75 for the lower, main cloud and values between 0.4 and 1 for the haze (varying between dark and bright, cloudy regions). Both particles were assumed to have a simple Henyey-Greenstein phase function, with asymmetry parameter $g = 0.6 - 0.7$. The analysis, and quality of fit to these Gemini/NIFS data, was greatly improved by Irwin et al. (2014) who made use of the newer WKMC-80K line database (Campargue et al. 2012) and who also applied an empirically derived single-scattering albedo spectrum for the Tropospheric Cloud, with the single-scattering albedo reducing with wavelength from 0.8 to 0.6 across the measured spectral range. With the new WKMC-80K generated k-tables and the modified scattering properties, Irwin et al. (2014) found that the simple 2-thin-cloud layer model still provided a very good fit to the observed spectra they analysed, even when compared to a model where a continuous vertical distribution of cloud particles was assumed, although the requirement for the Haze layer to be thin was found not to be strong.

Most recently, Irwin et al. (2015), analysing IRTF/SpeX observations of Neptune's sister planet, Uranus, have developed a novel retrieval technique whereby, in addition to the cloud opacity and vertical position, the imaginary refractive index spectrum of a cloud is retrieved. This can then be used in a Kramers-Kronig analysis to estimate the real component of the refractive index and from this complex refractive index spectrum can be computed self-consistent extinction cross-section, single-scattering albedo and phase

function spectra using Mie scattering. To analyse these VLT Neptune spectra we adopted the same approach, assuming *a priori* particle sizes of 1.0 μm (with variance 0.05) for both the tropospheric cloud and haze, and *a priori* refractive indices of $1.4 + 0.001i$ at all wavelengths. As described by Irwin et al. (2015) the condensates in Uranus' (and Neptune's) atmospheres are very unlikely to be liquid and thus spherical, as is assumed for Mie theory. However, Mie theory provides a reasonable first approximation to the scattering characteristics of an array of randomly orientated non-spherical particles, provided that features such as the 'rainbow' and 'glory', which can only be produced by spherical particles, are removed from the phase function spectra. This was done by fitting double Henyey-Greenstein phase functions to the Mie-calculated phase functions, where the phase function is represented by the asymmetry factors of the forward and backward scattering peaks, g_1 and g_2 and the fraction of forward scattering, f.

3.4. Cloud Retrievals

To determine the effectiveness of this new retrieval technique for Neptune, in a case where deep discrete clouds are visible, we chose to analyse the 'OB34' H-band cube (Table 1), recorded on October 12th 2013, which has a clearly visible deep cloud, just south of the main southern cloud belt (Fig. 4). Data from the pixels in a line passing through this cloud were extracted (Fig.9) and used as input to the retrieval model.

Following our previous Neptune modelling work, we initially attempted to fit the observations with a simple two-cloud model, with variable imaginary refractive index spectra for both layers. The *a priori* Tropospheric Cloud and Haze were based at 2 bar and 0.08 bar respectively and both had a fixed fractional scale height of 0.1. Although this model fitted most observed spectra very well, we were unable to fit the data to within the predicted random error of the VLT reductions and so additional noise was added to

account for 'forward-modelling error' to bring the final $\chi^2/n \sim 1$. Such forward-modelling error may arise from uncertainties in the spectral absorption data, and the various other assumptions that go into constructing a radiative-transfer model. Figure 10 shows the fit we can achieve with this model at near-equatorial latitudes (in this case 24.1°S), away from the main cloud belts, where the Haze opacity is low. As can be seen the fit is at most wavelengths extremely good. For reference Fig.10 also shows the spectrum calcuated with: 1) the Haze removed; 2) the Tropospheric Cloud removed; and 3) when both Haze and Tropospheric Cloud are removed, leaving only the reflectivity resulting from Rayleigh scattering from the air itself. As expected, it can be seen that reflection from the Haze is mostly responsible for the modelled reflectivity at methane-absorbing wavelengths, while the reflection from the deeper Tropospheric Cloud (TC) is important in regions where methane is more transparent. The retrieved cloud/haze opacity profiles and imaginary refractive index spectra of the cloud and haze particles are shown in Fig.11. The imaginary refractive index spectrum of the TC particles is almost identical to that derived for Uranus' tropospheric clouds by Irwin et al. (2015) and is reasonably well constrained (i.e. the retrieved errors are significantly smaller than the *a priori* errors). However, the Haze imaginary refractive index spectrum has barely moved from its *a priori* and the retrieved errors are not significantly smaller than the *a priori* errors, indicating that the spectral properties of the Haze are not well determined. Hence, the Haze refractive index spectrum was fixed to $1.4 + 0.001i$ at all wavelengths in subsequent retrievals, unless stated otherwise.

While the fit at 24.1°S is very good, at other latitudes the fit with a two-cloud model is significantly worse. This can be seen in Fig.12, which shows the fit at 38.5°S, where χ^2/n is greatest. Clearly there is something missing in our assumed two-cloud model at this location. Looking at the differences between the measured and modelled spectra, the difference seemed to be caused by missing reflection from a level between $2-3$ bar and 1 bar. We surmised that this might be due to a missing methane cloud. Using the assumed

temperature/abundance profile, we determined that such a cloud must be based at 1.44 bar and we added a thin cloud, based at this pressure level, assumed to be composed of methane ice particles. To model the reflectivity of these particles we used the complex refractive indices of Martonchik et al. (1994) and assumed a standard Gamma size distribution with mean radius $r = 1.2\mu$m and variance $= 0.1$. This size distribution was the same as that chosen to model the Upper Tropospheric Cloud of Uranus by Sromovsky et al. (2011), which was also used by Irwin et al. (2015) and Irwin et al. (2016) to model Uranus' methane cloud. We assume here that the methane clouds of Uranus and Neptune have similar size distributions. Figs.10 and Figs.12 show the result of adding this extra cloud to our best and worst fitting cases. As can be seen the improvement in our best test case at 24.1°S (Fig.10) is minimal (in fact it is very slightly worse), but the improvement at 38.5°S is very significant and clearly indicates that in the region where deep discrete clouds are visible, additional opacity is required that would appear to be consistent with the presence of a methane ice cloud.

Having considered two test cases, we then applied our retrieval model to all the pixels in the line passing through the deep cloud feature. Figure 13 shows the variation in the retrieved cloud/haze opacities and base pressures as a function of latitude along the sampled line of observation 'OB34' (Fig.9), plotted as a function of latitude using either the two-cloud or three-cloud models, depending on which fits better. Only retrievals at latitudes between the northernmost latitude observable (40°N) and 55°S have been plotted; accurate assignment of viewing geometries is difficult for pixels south of 55°S at this spatial resolution. The χ^2/n of the fit of both models is shown in the bottom right panel of Fig.13. In these retrievals the *a priori* tropospheric cloud particles' complex refractive index was set to $1.4 + 0.001i$ at all wavelengths. The haze particles' complex refractive indices were also set to $1.4 + 0.001i$ at all wavelengths, but fixed since Fig.11 showed we have very little sensitivity to spectral properties of these particles, assuming that they are highly scattering.

We can see that the two-cloud model gives a better fit at most latitudes, and the addition of methane clouds is only necessary at certain locations, here at the southern edge of the main southern mid-latitude cloud belt as we saw in Fig.12. At most other locations, adding a methane cloud actually worsens χ^2/n, suggesting that cross-correlation errors within the scheme, probably arising from the fact that the methane cloud becomes indistinguishable from the main cloud when its opacity is low, prevents the model from reaching as good a solution as if the methane cloud were omitted altogether. Apart from at 38.5°S, where the fit is significantly improved by adding a methane cloud, the only other locations where adding a methane cloud improves the fit is near 5°S and 15°S. However, at these locations the improvement in χ^2/n is actually very small and the presence of a methane cloud can be discounted. For reference, the errors on the retrieved opacities in Fig. 13 are of the order of 5% and 2% for the cloud and haze, respectively, at all latitudes, while the error on the retrieved opacity of the methane cloud, where it is detected, is approximately 5%. For the pressure levels shown in the panel B) of Fig.13, the base pressure of the Tropospheric Cloud at $\sim$ 2 bars is well constrained to within $\sim$ 0.1 bar, while the pressure of the methane cloud is fixed at 1.44 bar. The error on the Haze pressure is more problematic since with the *a priori* base pressure at $\sim$ 0.1 bar the transmission to space is effectively unity at all wavelengths and thus there is very little sensitivity to the precise pressure level (Fig.1). Hence, the retrieval does not stray far from the *a priori* except towards the northern edge of the line, where the longer path lengths corresponding to the higher zenith angles leads to some discrimination, and we find that the Haze base pressure needs to decrease. It is possible that the Haze lies at pressures less than $\sim$ 0.1 bar at all latitudes, but without observations at wavelengths where methane is more absorbing (for instance in the K-band) this cannot be determined. Finally, it should be noted that refractive index spectra very similar to those shown in Fig.11 were retrieved for the Tropospheric Cloud particles at all locations and in all subsequent cases reported in this paper.

3.5. Limb-darkening Considerations

Figure 13 shows a steady decrease of the opacity of the main Tropospheric Cloud deck from the cloudy southern zone (at $30 - 40°$S) towards the northern edge of the sampled line. We wondered whether this effect was physical or perhaps a geometrical effect of looking at increasingly high zenith angle. We thus revisited the required scattering properties of the Haze. From the same 'cube' we extracted all observations between $5 - 15°$S, plotted them as a function of zenith angle and extracted the general limb-darkening/limb-brightening curves at all wavelengths. We found these curves to be essentially identical to those determined from our previous study of Gemini/NIFS near-equator observations made in 2009 (Irwin et al. 2011), in which we showed that the Haze must be considerably non-scattering to avoid limb brightening at all wavelengths. In this previous Gemini/NIFS study we compared observed and modelled limb-darkening curves at just a few wavelengths and a limited set of assumed Haze scattering properties. We found that Haze particles having a single-scattering albedo, $\varpi \sim 0.4$ and Henyey-Greenstein phase function with asymmetry parameter, g, in the range 0.6 to 0.7 were most consistent with observations. With our new self-consistent cloud retrieval scheme we reanalysed the limb-darkening at 20 wavelengths spread evenly across the 1.47 to 1.71 μm range. At each wavelength, the limb-darkening observations were averaged and fitted with smooth reflectance versus emission angle curves, and sampled at four zenith angles between 0 and $65°$ (Fig.14), corresponding to the first four zenith angles of our five-zenith angle quadrature scheme. Since we had previously (Irwin et al. 2011) found that we need the Haze particles to be quite dark at equatorial latitudes, we revised the Haze *a priori* refractive indices from $1.4 + 0.001i$ to $1.4 + 0.3i$ (at all wavelengths) to lower the *a priori* single-scattering albedo to the low values found by Irwin et al. (2011), and fitted the opacity of the Tropospheric Cloud (TC) and Haze, the imaginary refractive index spectra of both the TC and Haze, and the TC and Haze particle sizes. For this limb-darkening analysis, starting with a less scattering Haze *a priori*

we found that we were sensitive to the refractive indices of both Haze and Tropospheric Cloud and we retrieved good limb-darkening curves at all wavelengths as can be seen in Fig.14. The particle scattering properties deriving from the retrieved refractive index spectra and particle sizes can be seen in Fig.15. As we can see the Tropospheric Cloud is found to be almost entirely forward scattering, with scattering asymmetry $g_1 \sim 0.7$, and has a single scattering albedo varying between 1 and 0.5 across the range. For the Haze we find that the particles are considerably darker than determined by Irwin et al. (2011), but the phase function is also substantially different, approaching Rayleigh-scattering. However, we believe this solution to be more reliable than our previous conclusions since this combination of properties was derived in a self-consistent manner instead of being chosen from a limited set of self-inconsistent properties in our previous work (Irwin et al. 2011), where this combination was never explored. Fig.16 shows the retrieved cloud/haze opacity profiles and retrieved imaginary refractive indices from this analysis at $5-15°$S. In this case we can see that the imaginary refractive index spectra of both the TC and Haze are well constrained at the wavelengths sensitive to these particles since the retrieved errors are significantly smaller than *a priori*. The position of the cloud/haze decks is almost indistinguishable from our retrievals with a highly scattering Haze *a priori* as is the retrieved refractive index spectrum of the Tropospheric Cloud. To determine whether we would find substantially different latitudinal variations using a low-scattering Haze *a priori*, we repeated our retrievals of the N/S strip through the deep cloud seen in 'OB34', but instead set the *a priori* Haze refractive indices to be $1.4 + 0.3i$ at all wavelengths and retrieved the cloud opacities for the Tropospheric Cloud, methane cloud (for the three-cloud model only) and Haze, and the refractive index spectra of both the TC and Haze for the two-cloud and three-cloud models. We found these models (Fig.17) had similar fitting accuracies at most locations to the retrievals shown in Fig.13 for the highly scattering *a priori* Haze, but that a poor fit was achieved in the cloudy zones at $30–40°$ N and $30–40°$S

for the two-cloud model. Note that in Fig.17 we again plot the fitted parameters of model that has the lowest χ^2/n at each latitude. The three-cloud model was able to significantly improve the fit at at 30–40° N, but had a similarly poor fit at 30–40° S. For both two-cloud and three-cloud models we found that we needed a far greater opacity of Haze to achieve the same levels of reflectivity from the upper troposphere/lower stratosphere, as might be expected, but that the increased absorption of this Haze worsened the model's ability to fit the reflected spectrum from the lower clouds. Although the retrieval model lowered the imaginary refractive indices of the Haze (as is indicated in Fig.17), and thus increased the single-scattering albedos of these particles over the mid-latitude cloudy zones, the relative weights in our retrieval set-up (and absence of limb-scattering constraints at higher latitudes) meant that the Haze particles did not become scattering enough to avoid having extremely large opacities at mid-latitudes. The marked increase of haze single-scattering albedo in the cloudy zones was also a conclusion of our previous Gemini/NIFS study (Irwin et al. 2011). Comparing the latitudinal variation in the retrieved opacity of the Tropospheric Cloud with that obtained for a highly scattering Haze *a priori* (Fig.13), we found a very similar decrease of opacity running north from the southern cloudy zone at 30 – 40° until 20°N, but a divergence from the highly scattering *a priori* Haze case at higher latitudes. At these higher latitudes, (and high zenith angles) the increased opacity of the overlying less-scattering Haze made it necessary to greatly increase the TC opacity in order to match the observed spectra. The results suggest that a reliable estimate of how the opacity of the Tropospheric Cloud varies with latitude depends greatly on the assumed and/or modelled scattering characteristics of the overlying Haze. Alternatively, if we assume the Tropospheric Cloud has a similar opacity at all latitudes, this could in future be used to provide a constraint on the single-scattering albedo of the overlying Haze.

3.6. Intermediate-Level Equatorial Clouds

To examine the cloud structure of regions with 'intermediate-level' clouds (the yellowish regions in the false colour plots, where the cloud is visible in the F3.0 and F1.25 filters, but not in the F0.2 filter, indicating these clouds to lie at pressures between 1.25 and 0.2 bar), the observation 'OB37' (Table 1) was selected and a north/south strip selected through the centre of such a cloud (Fig.9). We ran NEMESIS on the selected spectra using the two-cloud and three-cloud models with fixed Haze refractive indices of $1.4 + 0.001i$; the results are shown in Fig.18. Here we see that our fitting accuracy, except in the centre of the intermediate-level level cloud at $10.7°N$, is similar to the 'OB34' retrievals. The addition of a methane cloud only improves the fit near $15°S$, but only insignificantly and in most cases significantly worsens the fit. In the centre of the 'intermediate-level' feature, the two-cloud model is clearly preferred. Here the opacity of the Tropospheric Cloud is seen to decrease (relative to the overall decrease from south to north) while the Haze opacity (which here accounts for the reflection from the 'intermediate cloud') increases and its base pressure increases from ~ 80 mb to 400-500mb. This worst fitting spectrum at $10.7°N$ is shown in Fig.19 and we can see that there is a systematic difference between the modelled and measured spectra. We performed a number of retrieval tests, for example, adding a CH_4 cloud and allowing both it and the Haze to be vertically extended. While allowing a CH_4 cloud, based at 1.44 bar, to be extended produced no noticeable improvement in the fit, allowing the Haze to be extended (giving it an *a priori* fractional scale height of 0.5 ± 0.1 with a higher *a priori* base pressure of 0.25 bar (compared with 0.08 bar before) produced a noticeably improved fit, which is also shown in Fig. 19. The results for the two-cloud and three-cloud models with the vertically extended Haze applied to all latitudes in the 'OB37' north/south strip are shown in Fig.20. For the two-cloud model, extending the Haze leads to a significantly improved fit near the 'intermediate-level' feature at $10.7°N$, but the improvement at other latitudes is marginal. However, the 'intermediate-level'

515 feature at 10.7°N is the only one where the Haze base pressure is required to be increased to

516 pressures ($\sim 300 - 400$ mbar, similar to the case where the Haze is assumed to be vertically

517 thin) where the observations are actually sensitive to the fractional scale height of the Haze

518 (Fig.1). The three-cloud model is again generally found to be less successful, especially near

519 the south pole, where considerable cross-correlation between different cloud parameters

520 made the retrieval unstable, leading to the solution not varying far from *a priori* resulting

521 in high χ^2/n values, as can be seen. Adding a methane cloud only marginally improves the

522 fit near 15°S and 25°N as can also be seen.

4.   Discussion

523

524   The clouds of Neptune can be seen from our observations to be comprised of four main

525 types: 1) the main deep Tropospheric Cloud (TC) at 2–3 bars composed, probably, of H_2S

526 (e.g. de Pater et al. (2014)), 2) the high altitude, highly reflective, high opacity clouds

527 seen in the mid-latitude bands at $30 - 40°$ N,S; 3) small, bright 'deep' clouds seen near

528 the south pole in 2009 and along the southern edge of the main $30 - 40°S$ in 2013; and 4)

529 'intermediate-level', vertically extended clouds, with base pressures of $\sim 300 - 400$mb at

530 low latitudes. These four cloud types are clearly distinguishable in our false colour plots

531 and also in our retrieved vertical cloud profiles.

532   The distribution and appearance of the high altitude, mid-latitude clouds at $30 - 40°$

533 N,S in 2013 (cloud type 2) seems very similar to that observed in 2009, but the distribution

534 of the small, bright 'deep' clouds (cloud type 3) is completely different. In 2013 no such

535 clouds were seen near the south pole, but instead such clouds appeared at the southern

536 edge of the $30 - 40°S$ region. Irwin et al. (2011) postulated that the deep sub-polar clouds

537 seen in 2009 might be linked to the offset sub-polar hotspots observed near 70°S at mid-IR

538 wavelengths (8.6 μm) by VLT/VISIR in September 2006 (Orton et al. 2007, 2012). These

hotspots, observed via stratospheric CH_4 emission, were ephemeral in nature between 2003 and 2010. This is in contrast to the general warming trend towards Neptune's summer pole that has been observed consistently in ground-based mid-IR datasets since 2003 (Fletcher et al. 2014), and which could be explained by subsidence and adiabatic-warming of the air within a summer stratospheric vortex. Orton et al. (2012) suggested that a high-latitude wave, excited by powerful dynamics at deeper tropospheric levels (e.g., convective activity), could be interacting with and perturbing the polar stratospheric vortex. Generation of warm stratospheric airmasses by vertically-propagating waves was also a suggested mechanism for the formation of Saturn's stratospheric anticyclone following its 2010-2011 tropospheric storm (Fletcher et al. 2012), hinting at a coupling between the sporadic sub-polar clouds observed in the troposphere and the offset polar hotspots observed in the stratosphere. However, simultaneous observations in the near- and mid-IR were only attempted once for Neptune, at southern summer solstice in 2005 (Hammel et al. 2007), and did not reveal a direct correlation between the two (although no sub-polar clouds were visible in the near-IR at the time). A simultaneous campaign of near-IR and mid-IR imaging at comparable spatial resolutions will be required to confirm this coupling between tropospheric and stratospheric activity. Whether such clouds are linked to mid-IR features or not, the more precise radiative transfer modelling enabled by improved methane line data and retrieval methods reveals that such discrete deep clouds (i.e. cloud type 3) are possibly methane ice condensation clouds, formed presumably in regions of rapid upwelling. The global meridional circulation of Neptune can be inferred through observations of upper tropospheric temperature (de Pater et al. 2014; Fletcher et al. 2014) and is believed to be rising at mid-latitudes and sinking at the equator and poles. The appearance of deep convection methane clouds at the edges of the main cloudy zones at $30 - 40°$ N,S is then perhaps only to be expected. How such clouds might appear near the south pole as they did in 2009, however, remains a mystery, as is their apparent absence along the southern edge of

the main $30 - 40°S$ cloud belt at that time. However, we have found in this study that the spectra of such 'deep' clouds is well-modelled by the addition of a methane condensation cloud at 1.44 bar (the expected condensation level for the assumed temperature-pressure profile). It should be noted, though, that the addition of such a methane condensation cloud does not generally improve the fit to Neptunian near-IR spectra and in many locations significantly worsens it.

For the high-altitude clouds themselves (i.e. cloud type 2), these appear to be based at around the 100 – 200 mb level and vary in single-scattering albedo with latitude. We find that they have higher albedo in the main cloud belts, but very low albedo and low opacity elsewhere, as previously determined by Irwin et al. (2011). We suggest that Neptune is generally covered by a dark 'sooty' haze layer at these pressure levels, which only become highly scattering and optically thick in regions of upwelling, where they are coated with freshly condensed material - again, presumably methane ice. As mentioned earlier, if we assume the Tropospheric Cloud has a similar opacity at all latitudes, then this assumption could be used to better constrain the single-scattering albedo of the overlying Haze. However, we shall leave such an analysis to a future study.

The 'intermediate-level' equatorial clouds (cloud type 4) were only seen by Gemini/NIFS (Irwin et al. 2011) near the morning terminator, and it was thus possible from these observations that these might be ephemeral features linked in position to the diurnal cycle. Our new observations show that these 'intermediate-level' clouds are uniformly distributed with local time at equatorial latitudes. In addition, because our observations were made near the start and end of Neptune's transit on three consecutive nights we can see that these features, and indeed all the others seen, do not evolve significantly during a single night. Indeed, the 'intermediate-level' clouds seem to last for several days, which since they reside at latitudes of relatively low latitudinal wind shear is perhaps not surprising. In

terms of the overall meridional circulation it is curious that the 'intermediate-level' clouds at $300 - 400$mb should appear at near-equatorial latitudes – a region generally thought to be one of subsiding air in the upper troposphere (de Pater et al. 2014). The situation is analogous to the appearance of convective plumes in Jupiter's North Equatorial Belt, an area similarly thought to be a region of generally subsiding air. It may be that in both 'belt' locations, conditional instabilities mean that small convective events can occur amongst otherwise descending air and, in the case of Neptune, lead to condensation that perhaps becomes vertically extended. The most obvious candidate for such condensation is, again, methane and it is thus puzzling that no 'deep' methane clouds have been seen at the equator, but instead only 'intermediate-level' level ones. Alternatively, it may be that the 'intermediate-level' clouds are caused by material descending and freezing out through the tropopause cold-trap as part of the overall upper tropospheric meridional circulation scheme indicated from mid-IR observations with air rising at mid-latitudes and sinking at the poles and equator (de Pater et al. 2014). This descending branch at the equator presumably weakens at pressures greater than 1 bar since Karkoschka and Tomasko (2011) find that methane is enriched at all latitudes equatorwards of $\sim 45°$N,S, indicating upwelling, and only decreases at more polar latitudes, possibly indicating subsidence, or decrease in convective overturning. This picture is also mirrored in radio images of Neptune (de Pater et al. 2014), which shows increased emission at the south pole, indicating dryer air at pressures greater than 10 bar, but do not show increased emission at the equator.

5. Conclusions

We have compared Integral Field Unit Spectrometer observations of Neptune made in 2013 with VLT/SINFONI, with Gemini/NIFS observations made in 2009 and 2011. We have shown that the small, deep, discrete clouds seen near Neptune's south pole in 2009

by Gemini/NIFS were absent in 2011 and 2013, but similar deep clouds appeared at the southern edge of the southern mid-latitude cloudy zone at 30–40°S region in 2013, which were not apparent in 2009 and 2011. Our observations, taken at the beginning and end of three consecutive nights show that the cloud features are not significantly deformed by latitudinal windshear during a single night. In particular, the 'intermediate-level' level clouds observed by Gemini/NIFS in 2009 (Irwin et al. 2011) do not appear to be limited in their distribution to be near the morning terminator, a possibility that could not be ruled out by the Gemini/NIFS observations, but instead can be seen to survive several transits across Neptune's disc.

We have analysed our new VLT/SINFONI H-band observations using a self-consistent cloud-retrieval model, previously applied to Uranus IRTF/SpeX observations by Irwin et al. (2015). This improvement in our retrieval technique, coupled with the use of greatly improved methane absorption data from Campargue et al. (2012) means that we can fit the observations to much higher precision and at greater spectral resolution, allowing us to extract more precise information from these data than was possible in our previous study of Gemini/NIFS H-band observations made in 2009 (Irwin et al. 2011). We find that a simple two-cloud model (a 'Tropospheric Cloud' near the 2–3 bar level and a 'Haze' based near 0.1 bar) recommended by Irwin et al. (2011) is sufficient to model the bulk of spectra across Neptune's disc at these wavelengths. The opacity of the Tropospheric Cloud is seen to vary slowly with latitude, while the 'Haze' optical depth varies greatly from being optically thin (and poorly scattering with low single scattering albedo) at most latitudes, to becoming optically thick and highly scattering in the bright mid-latitude belts at 30–40°N,S. At these locations we suggest that cloud (methane ice) is condensing on the background dark haze particles. However, we find that the discrete, bright, 'deep' clouds seen at the southern edge of the southern mid-latitude cloudy zone at 30–40°S are much better modelled by adding a methane cloud layer, based at the condensation level of 1.44 bar expected from

the assumed temperature-pressure-abundance profile. Hence, these features appear to be localised methane clouds, caused by rapid convection and condensation of material in the 1–1.5 bar region. For the 'intermediate-level' level clouds seen at more equatorial latitudes, we have shown that these clouds can again be modelled (as done in our previous analysis) with the two-cloud model, by lowering the base of the 'Haze' layer to the 300 – 400mb pressure level, but that we are unable to achieve as good a fit unless we allow the Haze layer to become vertically extended.

6. Acknowledgements

– 30 –

REFERENCES

de Bergh, C., Lutz, B.L., Owen, T., Brault, J., Chauville, J., 1986. Monodeuterated methane in the outer Solar System. II. Its detection on Uranus at 1.6 μm. ApJ, 311, 501 – 510.

Borysow, A., 1991. Modeling of collision-induced infrared absorption spectra of $H_2 - H_2$ pairs in the fundamental band at temperatures from 20 to 300 K. Icarus 92, 273 – 279.

Borysow, A., 1992. New model of collision-induced infrared absorption spectra of $H_2 - He$ pairs in the 2 – 2.5 μm range at temperatures from 20 to 300 K – An update. Icarus 96, 169 – 175.

Borysow, A., Frommhold, L., 1986. Theoretical collision-induced rototranslational absorption spectra for the outer planets – $H_2 - CH_4$ pairs. Astrophys. J. 304, 849 – 865.

Borysow, A., Frommhold, L., 1987. Collision induced rototranslational absorption spectra of CH_4CH_4 pairs at temperatures from 50 to 300 K. Astrophys. J. 318, 940 – 943.

Burgdorf, M., Orton, G.S., Davis, G.R., Sidher, S.D., Feuchtgruber, H., Griffin, M.J., Swinyard, B.M. 2003. Neptune's far-infrared spectrum from the ISO long-wavelength and short-wavelength spectrometers. Icarus, 164, 244 – 253.

Campargue, A., Wang, L., Mondelain, D., Kassi, S., Bzard, B., Lellouch, E., Coustenis, A., de Bergh, C., Hirtzig, M., Drossart, P., 2012. An empirical line list for methane in the 1.26 – 1.71 μm region for planetary investigations (T = 80 – 300 K). Application to Titan. Icarus, 219, 110 – 128.

Conrath, B.J., Gautier, D., Owen, T.C., Samuelson, R.E., 1993. Constraints on N_2 in Neptunes atmosphere from Voyager measurements. Icarus, 101, 168 – 171.

Conrath, B.J., Gierasch, P.J., Ustinov, E.A., 1998. Thermal structure and para hydrogen fraction on the outer planets from Voyager IRIS measurements. Icarus 135, 501 – 517.

Cushing, M.C., Vacca, W.D., Rayner, J.T. 2004. Spextool: A spectral extraction package for SpeX, a 0.8 – 5.5 micron cross-dispersed spectrograph. Publ. of Ast. Soc. Pacific 116, 362 – 376.

Cutri, R.M. et al. 2003. 2MASS All Sky Catalog of point sources. The IRSA 2MASS All-Sky Point Source Catalog, NASA/IPAC Infrared Science Archive.

de Pater, I., Fletcher, L.N., Luszcz-Cook, S., DeBoer, D., Butler, B., Hammel, H.B., Sitko, M.L., Orton, G., Marcus, P.S., 2014. Neptune's global circulation deduced from multi-wavelength observations. Icarus, 237, 211 – 238.

Fiorenza, C., Formisano, V. 2005. A solar spectrum for PFS data analysis. Plan. Space Sci. 53, 1009 – 1016.

Fletcher, L.N., Hesman, B.E., Achterberg, R.K., Irwin, P.G.J., Bjoraker, G., Gorius, N., Hurley, J., Sinclair, J., Orton, G.S., Legaretta, J., García-Melendo, E., Sánchez-Lavega, A., Read, P.L., Simon-Miller, A.A., Flasar, F.M. 2012. The origin and evolution of Saturn's 2011 – 2012 stratospheric vortex. Icarus, 221, 560 – 586.

Fletcher, L.N., de Pater, I., Orton, G.S., Hammel, H.B., Sitko, M.L., Irwin, P.G.J., 2014. Neptune at summer solstice: Zonal mean temperatures from ground-based observations, 2003 – 2007. Icarus, 231, 146 – 167.

Hammel, H.B., Sitko, M.L., Lynch, D.K., Orton, G.S., Russel, R.W. Geballe, T.R., de Pater, I. 2007. Distribution of ethane and methane emission on Neptune. AJ, 134, 637 – 641.

Hartmann, J.-M., Boulet, C., Brodbeck, C., van Thanh, N., Fouchet, T., Drossart, P., 2002. A far wing lineshape for H_2 broadened CH_4 infrared transitions. J. Quant. Spec. Radiat. Transf., 72, 117 – 122.

Irwin, P.G.J., Fletcher, L.N., Read, P.L., de Pater, I., Orton, G.S., Teanby, N.A., & Davis, G.R. 2016. Spectral analysis of Uranus' 2014 bright storm by VLT/SINFONI. Icarus, 264, 72 – 89.

Irwin, P.G.J., Tice, D.S., Fletcher, L.N., Barstow, J.K., Teanby, N.A., Orton, G.S. & Davis, G.R. 2015. Reanalysis of Uranus' cloud scattering properties from IRTF/SpeX observations using a self-consistent scattering cloud retrieval scheme. Icarus, 250, 462 – 476.

Irwin, P.G.J., Lellouch, E., de Bergh, C., Courtin, R., Bézard, B., Fletcher, L.N., Orton, G.S., Teanby, N.A., Calcutt, S.B., Tice, D., Hurley, J., & Davis, G.R. 2014. Line-by-line analysis of Neptune's near-IR spectrum observed with Gemini/NIFS and VLT/CRIRES. Icarus, 227, 37.

Irwin, P.G.J., Teanby, N.A., Davis, G.R., Fletcher, L.N., Orton, G.S., Tice, D., Hurley, J., Calcutt, S.B. 2011. Multispectral imaging observations of Neptune' s cloud structure with Gemini-North. Icarus, 216, 141 – 158.

Irwin, P.G.J., Teanby, N.A., de Kok, R., Fletcher, L.N., Howett, C.J.A., Tsang, C.C.C., Wilson, C.F., Calcutt, S.B., Nixon, C.A., & Parrish, P.D. 2008. The NEMESIS planetary atmosphere radiative transfer and retrieval tool. J. Quant. Spec. Radiat. Transf.109, 1136.

726 Karkoschka, E., Tomasko, M., 2010. Methane absorption coefficients for the jovian planets
727   from laboratory, Huygens, and HST data. Icarus, 205, 674 – 694.

728 Karkoschka, E., Tomasko, M., 2011. The haze and methane distributions on Neptune from
729   HST–STIS spectroscopy. Icarus, 211, 780 – 797.

730 Lacacheux, A., Zarka, Ph., Desch, M.D., Evans, D.R. 1993. The sidereal rotation period of
731   Neptune. Geophys. Res. Lett., 20, 2711 – 2714.

732 Lacis, A.A., Oinas, V., 1991. A description of the correlated-k distribution method for
733   modelling nongray gaseous absorption, thermal emission, and multiple scattering in
734   vertically inhomogeneous atmospheres. J. Geophys. Res., 96, 9027 – 9063.

735 Lellouch et al. 2011. First results of Herschel-PACS observations of Neptune. A&A, 518,
736   L152.

737 Lindal, G.F., 1992. The atmosphere of Neptune: An analysis of radio occultation data
738   acquired by Voyager 2. AJ, 103, 967 – 982.

739 Martonchik, J.V., Orton, G.S., 1994. Optical constants of liquid and solid methane. Appl.
740   Opt. 33, 8306 – 8317.

741 Orton, G.S., Encrenaz, T., Leyrat, C., Puetter, R., Friedson, A. J., 2007. Evidence for
742   methane escape and strong seasonal and dynamical perturbations of Neptune's
743   atmospheric temperatures. A&A, 473, L5 – L8.

744 Orton, G.S., Fletcher, L.N., Liu, J., Schneider, T., Yanamandra-Fisher, P., de Pater, I.,
745   Edwards, M.. Geballe, T.R., Hammel, H.B., Fujiyoshi, T., Encrenaz, T., Pantin, E.,
746   Mousis, O., Fuse, T., 2012. Recovery and characterization of Neptune's near-polar
747   stratospheric hot spot. Planet. Space Sci., 61, 161 – 167.

Plass, G.N., Kattawar, G.W., Catchings, F.E., 1973. Matrix operator method of radiative transfer. 1: Rayleigh scattering. Appl. Opt. 12, 314 – 329.

Sromovsky, L.A., Fry, P.M., Kim, J.H., 2011. Methane on Uranus: The case for a compact CH_4 cloud layer at low latitudes and a severe CH_4 depletion at high latitudes based on a re-analysis of Voyager occultation measurements and STIS spectroscopy. Icarus215, 292 – 312.

Sromovsky, L.A, Limaye, Fry, P.M. 1993. Dynamics of Neptune's major cloud features. Icarus, 105, 110 – 141.

Vacca, W.D., Cushing, M.C., Rayner, J.T. 2003. A Method of Correcting Near-Infrared Spectra for Telluric Absorption. Publ. of Ast. Soc. Pacific 115, 389 – 409.

Zheng, C., Borysow, A., 1995. Modeling of collision-induced infrared absorption spectra of H_2 pairs in the first overtone band at temperatures from 20 to 500 K. Icarus 113, 84 – 90.
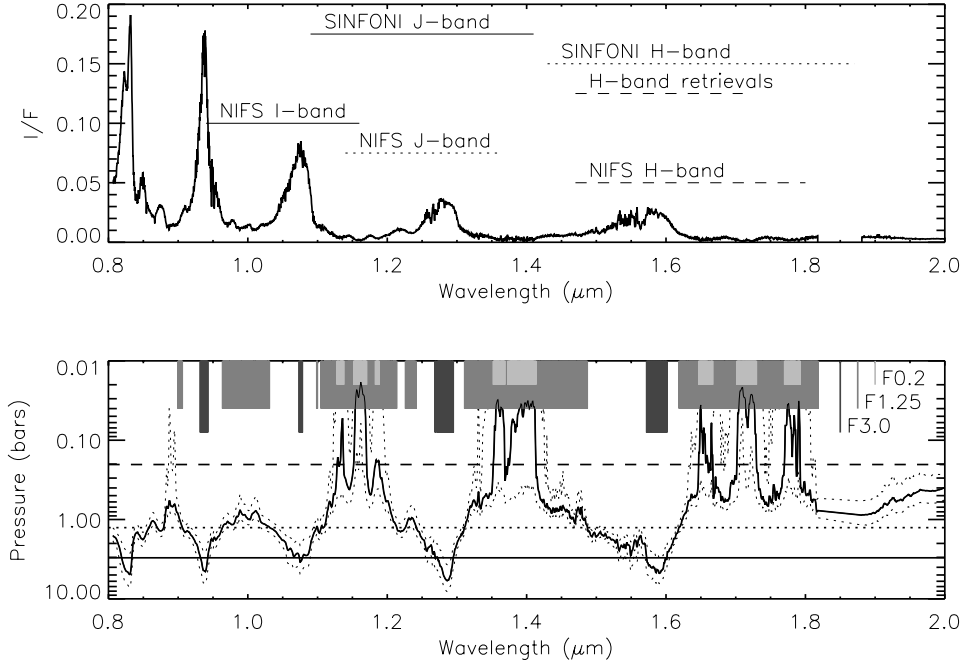
Fig. 1.— Top panel shows a typical I/F spectrum of Neptune as observed by IRTF/SpeX, together with the wavelengths spanned by selected VLT/SINFONI and Gemini/NIFS grisms. Bottom panel shows the pressure level in Neptune's atmosphere at which two-way transmission to space is 0.5 for a cloud-free atmosphere. Overplotted in the bottom panel are the pressure levels (dotted lines) for which the two-way transmission to space is 0.25 and 0.75, giving an indication of the vertical resolution of the observations at a single wavelength. Also overplotted in the bottom panel are the chosen cut-off pressures of 3, 1.25 and 0.2 bar. Continuum images ('F3.0') are averaged over all wavelengths where the transmission to 3 bars exceeds 0.5. Medium-absorption and high-absorption images are averaged over all wavelengths where the transmission at 1.25 and 0.2 bars is respectively less than 0.5, labelled respectively as 'F1.25' and 'F0.2'. The wavelengths selected by these filters in the wavelength range (0.9 − 1.87 μm) are indicated by the grey regions in the bottom panel of differing length and greyness, indicated by the vertical bars in the top right of the bottom panel.
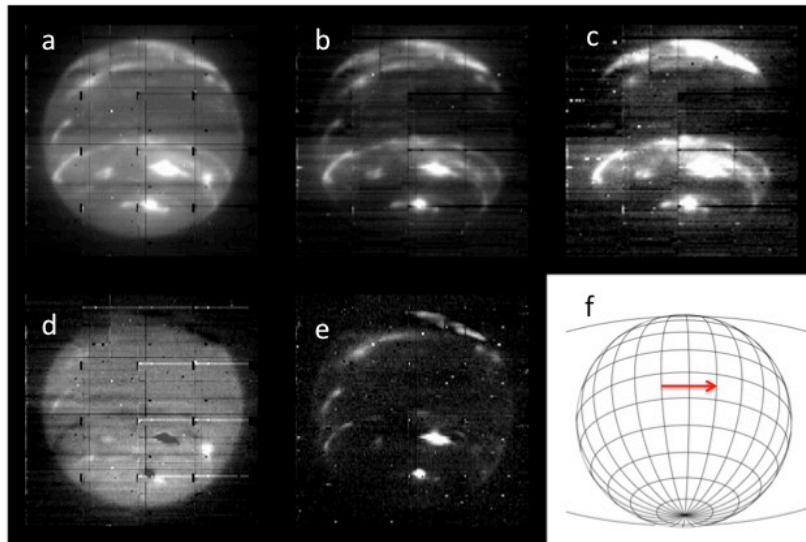
Fig. 2.— One of the best H-band observations of 12th October 2013 (OB36), formed of a 4×4 mosaic of $0.025''$plate scale cubes. The top row shows the appearance of Neptune in the different wavelength 'filters'. Panel (a) shows the planet at wavelengths where the two-way transmission to space, for a cloud-free atmosphere, exceeds 0.5 at the 3-bar level (i.e. the 'F3.0' filter). Panel (b) shows the planet at wavelengths where the two-way transmission to the 1.25 bar level is less than 0.5 ('F1.25'), while panel (c) shows the planet at wavelengths where the two-way transmission to the 0.2-bar level is less than 0.5 ('F0.2'), which is only sensitive to the hazes at pressures less than 0.2 bar. The bottom row shows differences between the images to highlight the clouds at different levels. Panel (d) shows the F3.0 image (Panel (a)) minus the F1.25 image (Panel (b)) and shows the distribution of cloud reflectivity at the main cloud deck at $\sim 1 - 3$ bars, while panel (e) shows the F1.25 image (Panel(b)) minus the F0.2 image (Panel (c)), showing the distribution of clouds between roughly 1.25 and 0.2 bar. Panel (f) shows a projection of Neptune's disc and ring for reference. The dark patches in Panel (d) do not indicate holes in the deep cloud, only that the scaling chosen to eliminate the reflectivity of overlying clouds leads to slightly too much reflectivity being subtracted in cases where the overlying clouds are very thick. Neptune's sense of rotation is indicated by the arrow in panel (f).
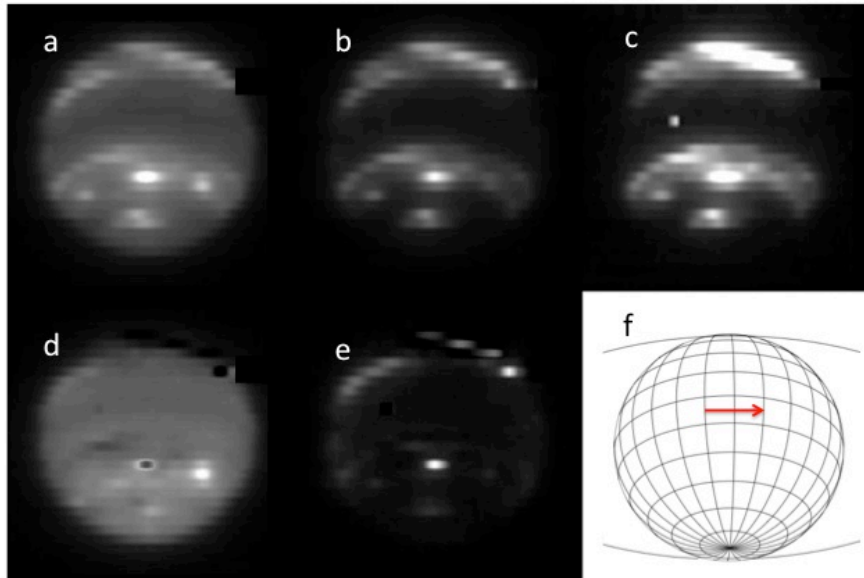
Fig. 3.— Lower-resolution H-band observation $(0.1''$ plate scale) made on 12th October 2013 (OB34), recorded shortly before OB36 (Fig.2). The layout of the figure is identical to Fig.2.
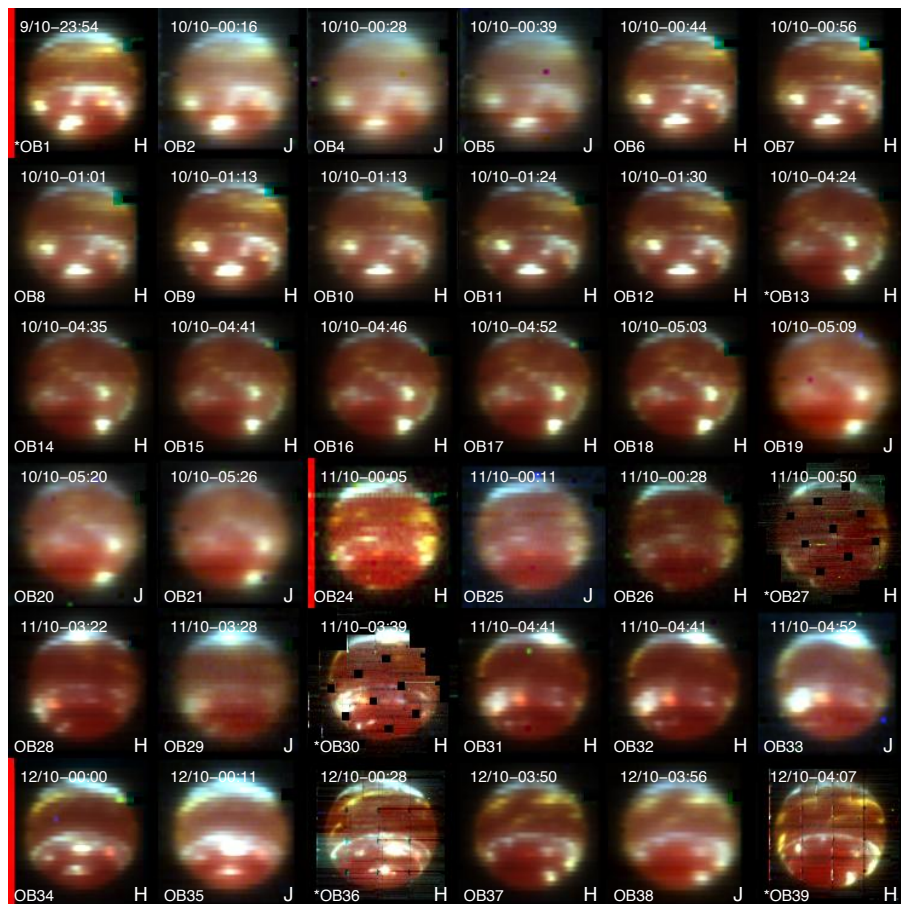
Fig. 4.— Summary of October 2013 VLT/SINFONI H- and J-band Neptune observations, gridded with time running from top left to bottom right. The observation date/time and grism are indicated by each image. The starting image from each night is indicated by the red bar on the left hand edge side of the image. Images are plotted in false colour, where red is the continuum F3.0 image (i.e. panel (a) in Figs. 2, 3), green is the F1.25 image where $\text{Trans}_{1.25bar} < 0.5$ (i.e. panel (b) in Figs. 2, 3) and blue is the F0.2 image where $\text{Trans}_{0.2bar} < 0.5$ (i.e. panel (c) in Figs. 2, 3). In this scheme, deep clouds appear red, intermediate-level clouds appear yellow and high hazes appear bluish. Bright 'white' (and thus high) clouds are seen at mid-latitudes in both hemispheres, with lower altitude clouds seen at more equatorial latitudes. No discrete deep (indicated as 'red') clouds are seen near the south pole, but such clouds are visible near the southern edge of the southern equatorial cloudy zone. Images selected for the 'scan' plot, shown in Fig.5 are indicated by the '*' symbol to the left of the observation name.
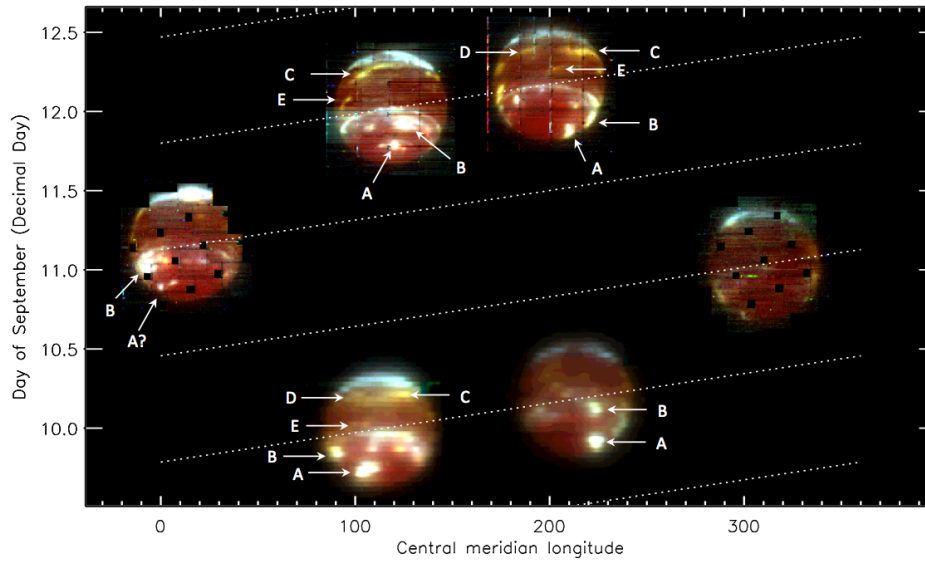
Fig. 5.— Scan plot of selected 2013 VLT/SINFONI H-band observations made in October 2013. The images are plotted at a point depending on the central meridian longitude of the observation (assuming a rotation rate of 16.11 hours) and the observation time plotted as the digital day of the month i.e. October 10th at 00:00 UT is 10.0). Images with best resolution have been chosen covering as great a time period as possible. The diagonal dotted lines indicate how the central meridian longitude varies with time. Distinct identifiable features have been labelled: A) sub-polar discrete cloud; B) mid-latitude bright cloud; C, D and E) near-equatorial intermediate level clouds. The approximate planetocentric latitudes of the five labelled features are 67°S, 42°S, 12°N, 12°N, and 9°S, respectively.
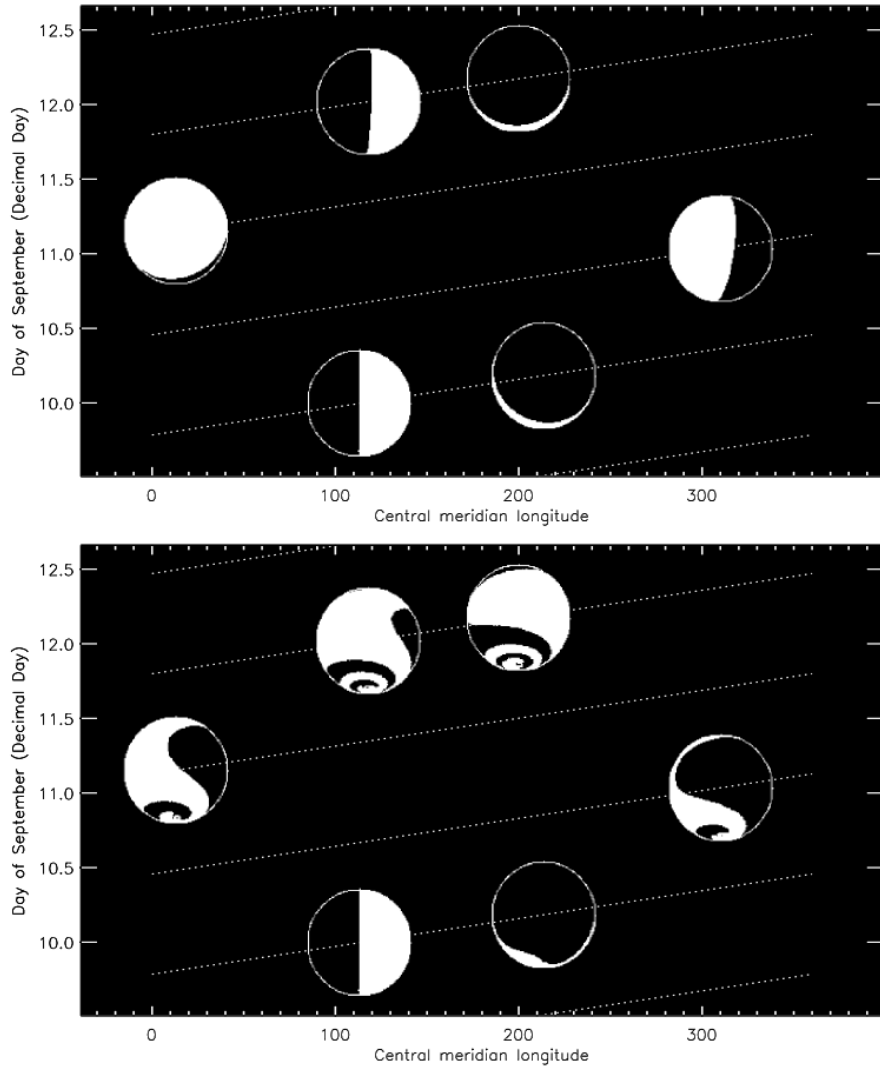
Fig. 6.— For the same time period as is presented in Fig.5, the top plot shows how Neptune would appear with a cloud distribution that is white in one hemisphere and dark in the other if the latitudinally different rotation rates are neglected. The terminator is set to be at a longitude of 0° with white on the right hand side at the time of the first observation plotted. The bottom plot shows how the appearance of such a distribution would be distorted by the very different rotation rates seen at different latitudes in Neptune's atmosphere due to the extreme latitudinal variation of zonal wind speed.
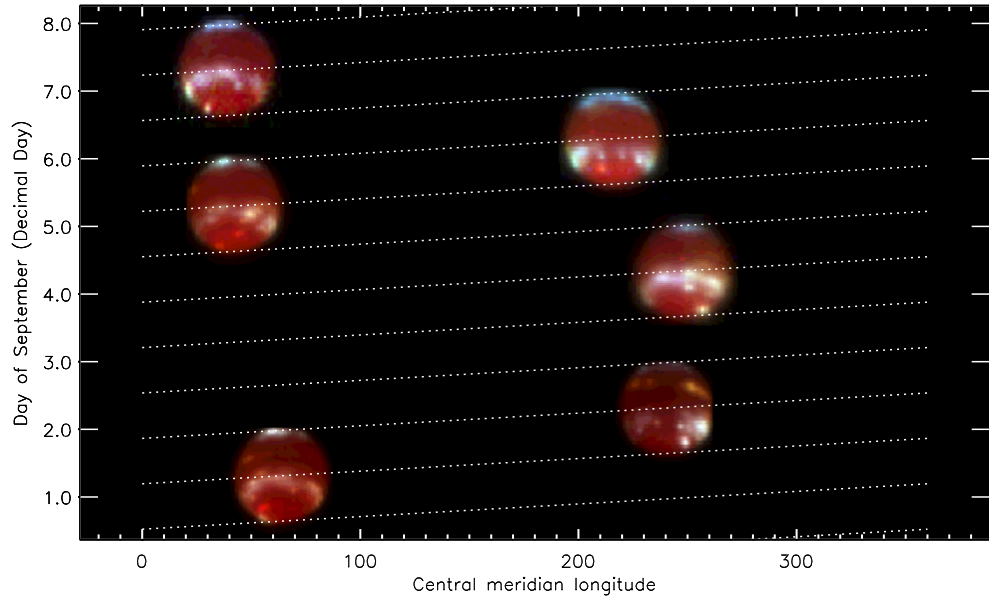
Fig. 7.— As Fig.5, but showing a scan plot of the 2009 Gemini/NIFS H-band observations during September 2009.
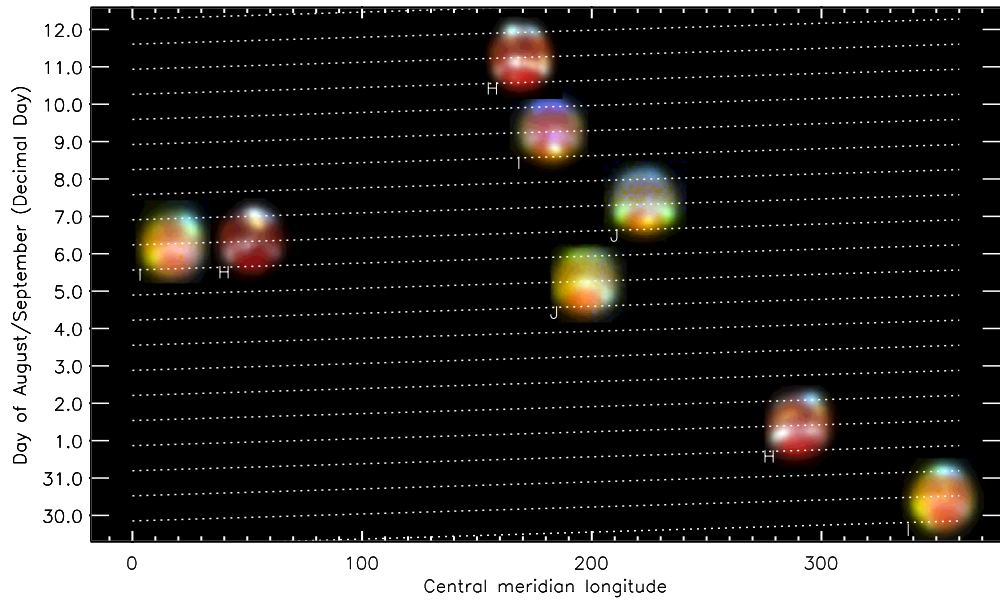

Fig. 8.— As Fig.5, but showing a scan plot of the 2011 Gemini/NIFS observations in the I-, J-, and H-bands during August/September 2011. The grism used for the observation is indicated by each image.
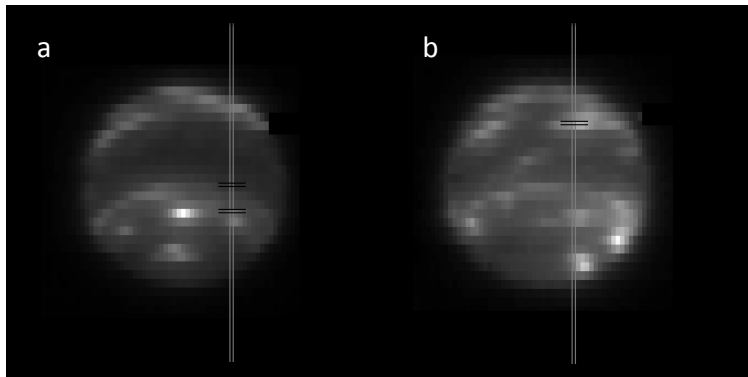
Fig. 9.— The two lines of pixels selected for H-band retrieval analysis. Panel (a) shows observation 'OB34' with line cutting through the deep cloud feature in southern hemisphere. Panel (b) shows observation 'OB37' with line cutting through the intermediate-level cloud just north of the equator. Figs. 10–13 and Fig.17 show the line retrievals for 'OB34', while Figs.18 – 20 show the line retrievals for 'OB37'. The locations highlighted by the black horizontal lines are those for which the retrieved spectra are presented in detail in Figs. 10, 12, and 19.
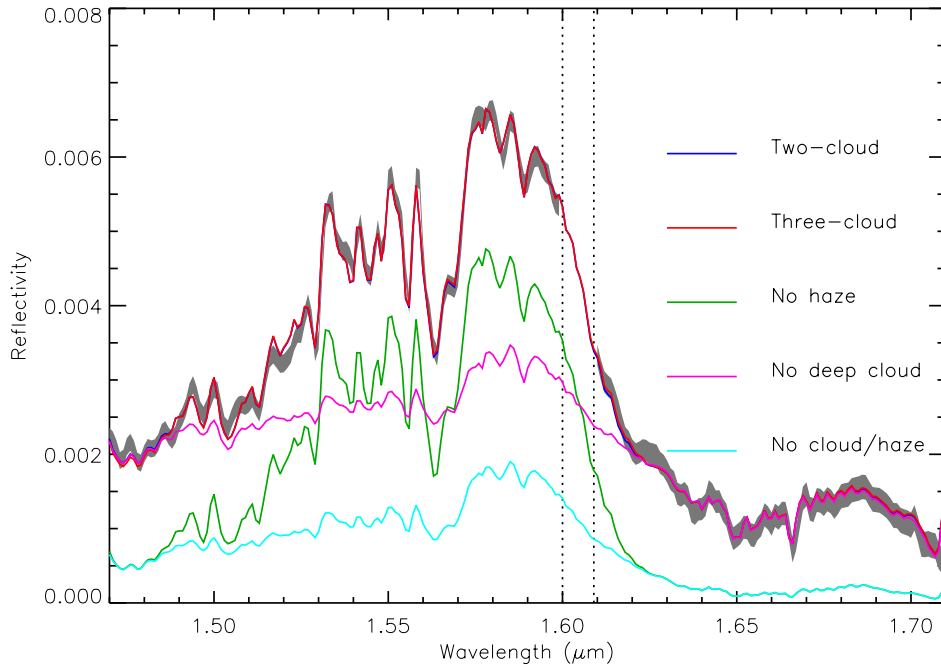
Fig. 10.— Retrieved spectra for a typical sample pixel at 24.1°S (the topmost indicated pixel in panel (a) of Fig.9), just north of the southern mid-latitude cloud belt, using a two-cloud and three-cloud model. The grey shaded region is the measured spectrum and errors, while the solid coloured lines are the retrieved spectra. At this latitude the two-cloud (blue) and three-cloud (red) models are effectively indistinguishable. For reference, also plotted are the spectra calculated for the two-cloud haze case: 1) when just the Haze is removed (green); 2) when just the Tropospheric Cloud is removed (mauve); and 3) when both cloud layers are removed (cyan), in which case the reflectivity calculated is due entirely to Rayleigh scattering. NB in this case data were missing between 1.6 and 1.61 μm.
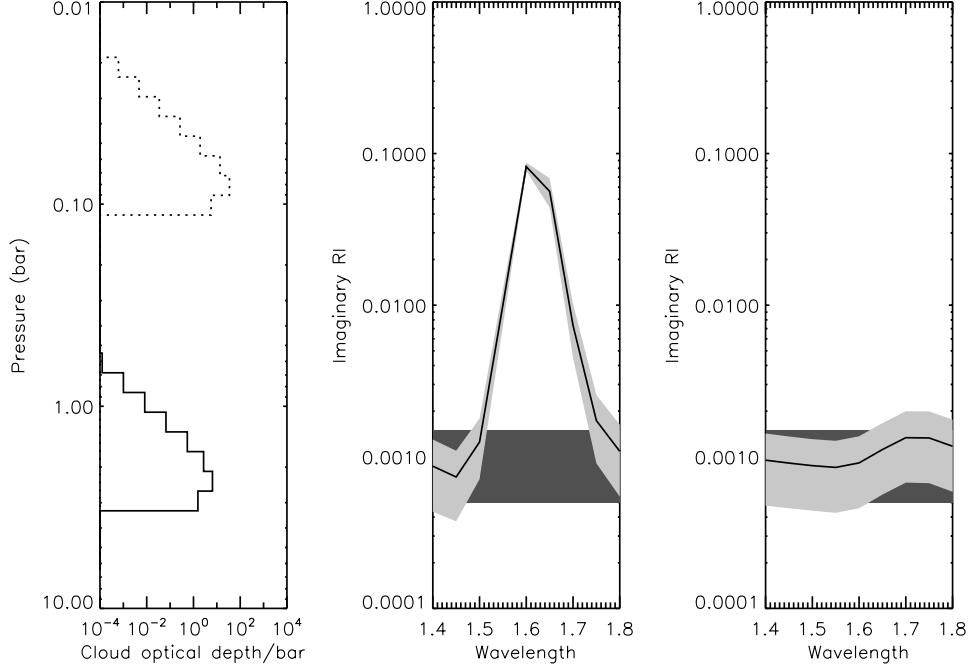
Fig. 11.— Retrieved cloud/haze opacity profile and imaginary refractive index spectra for the Tropospheric Cloud (TC) and Haze from the sample pixel at 24.1°S. Left hand panel shows the retrieved TC/Haze opacity profiles (solid line - TC, dotted line - Haze), while the middle and right hand panels show the retrieved imaginary refractive index spectra for the Tropospheric Cloud (middle panel) and Haze (right hand panel) respectively. For the imaginary refractive indices, the *a priori* value and range is indicated by the darker shaded region, while the retrieved spectra are indicated with the solid line and errors indicated by the lighter shaded region. The imaginary refractive index spectrum of the Tropospheric Cloud can be seen to be generally well-retrieved. However, the imaginary refractive index spectrum of the Haze has barely moved from the *a priori* and the retrieved errors are no smaller than *a priori*. Hence, we conclude that the imaginary refractive index spectrum of the Haze particles are not retrievable in this case.
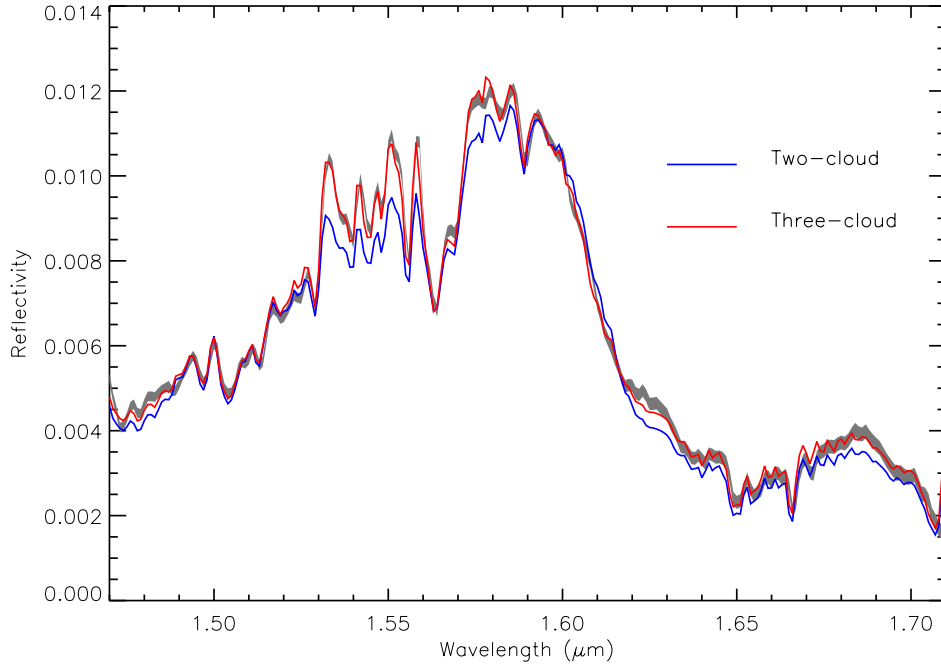
Fig. 12.— Retrieved spectra for sample pixel at 38.5°S (the lowermost indicated pixel in panel (a) of Fig.9, in the centre of the discrete 'deep' cloud feature), using a two-cloud (blue), and three-cloud (red) models, where our fit with the two-cloud model is worst. The form of the figure is identical to Fig. 10 and again the grey shaded region is the measured spectrum and errors, while the solid coloured lines are the retrieved spectra. The two-cloud model clearly gives a worse fit at this location, but the addition of a methane cloud based at 1.44 bar greatly improves the fit to the observed spectrum.
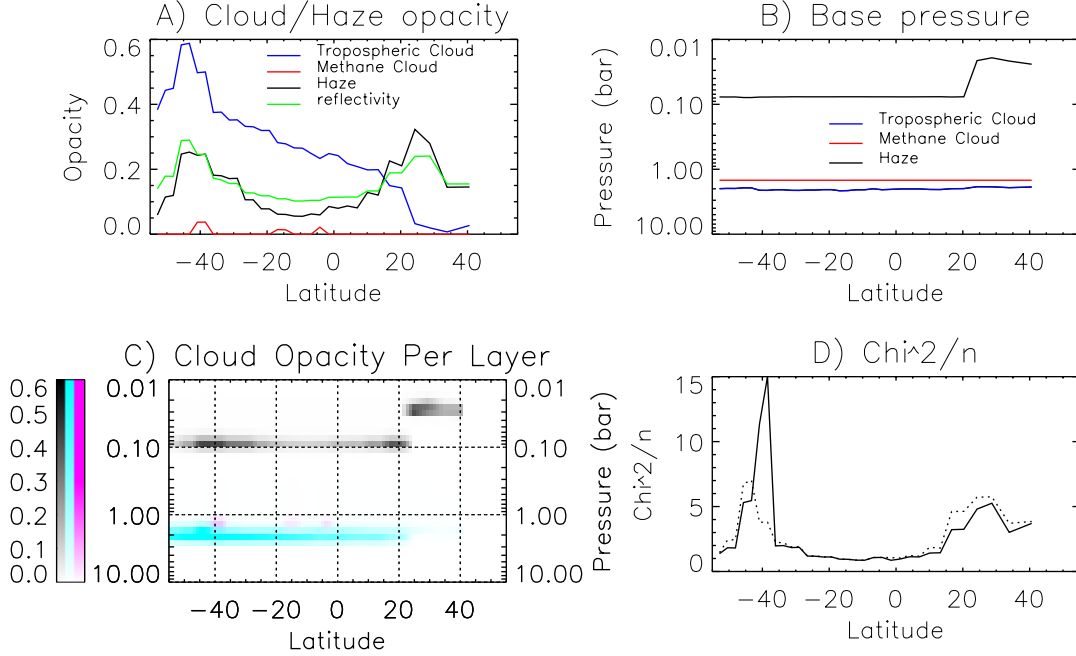
Fig. 13.— Retrieved cloud/haze opacities (Panel A) and base pressures (Panel B) as a function of latitude along the selected line for observation 'OB34' (Fig.9), together with an image representation of the resulting opacity per layer in the atmospheric model of each cloud type (Panel C) and the estimated χ^2/n of the fit for the three-cloud (dotted) and two-cloud (solid) models (Panel D). Where the three-cloud model fits better than the two-cloud model, its retrieved quantities have been plotted, otherwise the two-cloud model results are shown. Panel A also shows the observed reflectivity averaged between 1.57 and 1.6 μm to help identify the cloud features. In the cloud opacity per layer plot (Panel C), the opacity of the Haze is represented in grey, the opacity of the Tropospheric Cloud is coloured in cyan, and the methane cloud (where its addition is found to improve the fit) is coloured magenta. The χ^2/n for the two-cloud (solid line) and three-cloud (dotted line) models shown as the dotted line in Panel C, indicates that adding a methane cloud layer only improves the fit at certain locations. In these retrievals the *a priori* tropospheric cloud particles' complex refractive index was set to $1.4 + 0.001i$ at all wavelengths. The complex refractive index of the haze particles was also set to $1.4 + 0.001i$ at all wavelengths, but fixed since Fig.11 shows we have little sensitivity to the haze refractive index spectrum, assuming the *a priori* particles are highly scattering.
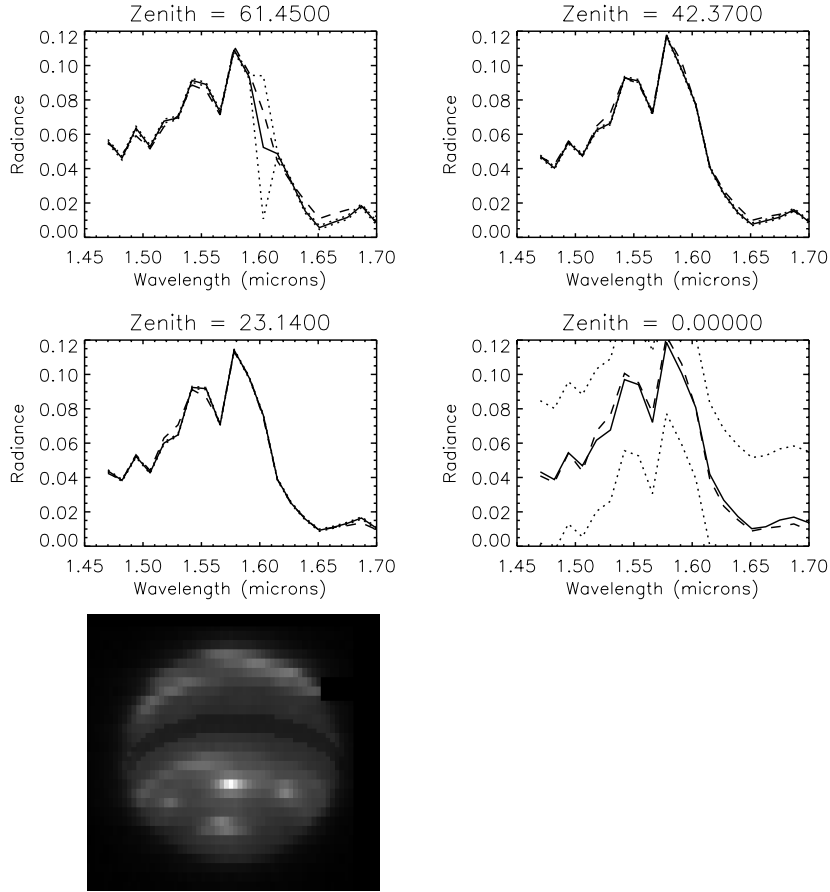
Fig. 14.— Latitude band (5 – 15°S) selected for limb-darkening analysis (bottom left) and extracted averaged spectra at the first four angles of the zenith-angle quadrature scheme. Solid lines and dotted lines indicate measured spectra and errors, while the dashed lines are the fitted spectra. Just twenty wavelengths were selected for this analysis. The larger measurement errors for zenith angle = 0 are to account for the fact that we have extrapolated the data beyond the range of measured zenith angles. However, the fit remains good. The larger measurement errors near 1.6 μm for zenith angle = 61.45° indicate missing data.
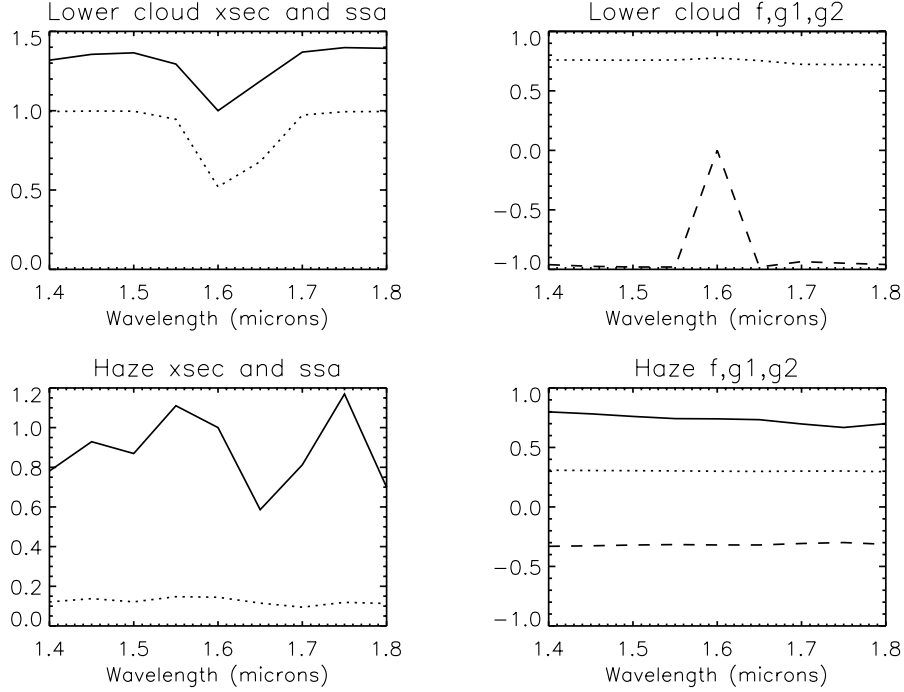
Fig. 15.— Derived scattering properties of the Tropospheric Cloud and Haze from the limb-scattering analysis at $5 - 15°S$ – extinction cross-section, single-scattering albedo, and Henyey-Greenstein phase function coefficients f, g_1 and g_2. For cross-section and single scattering albedo, the solid lines are the cross-sections, while dotted lines are single scattering albedoes. For the phase function parameters, f is indicated by the solid lines, g_1 is indicated by the dotted lines and g_2 are indicated by the dashed lines. These properties were derived from the fitted imaginary refractive index spectra and particle sizes. For the Tropospheric Cloud (TC) phase function parameters, f is effectively unity at all wavelengths. Mean particle sizes of 1.1 and 0.2 μm were retrieved for the TC and Haze particles respectively.
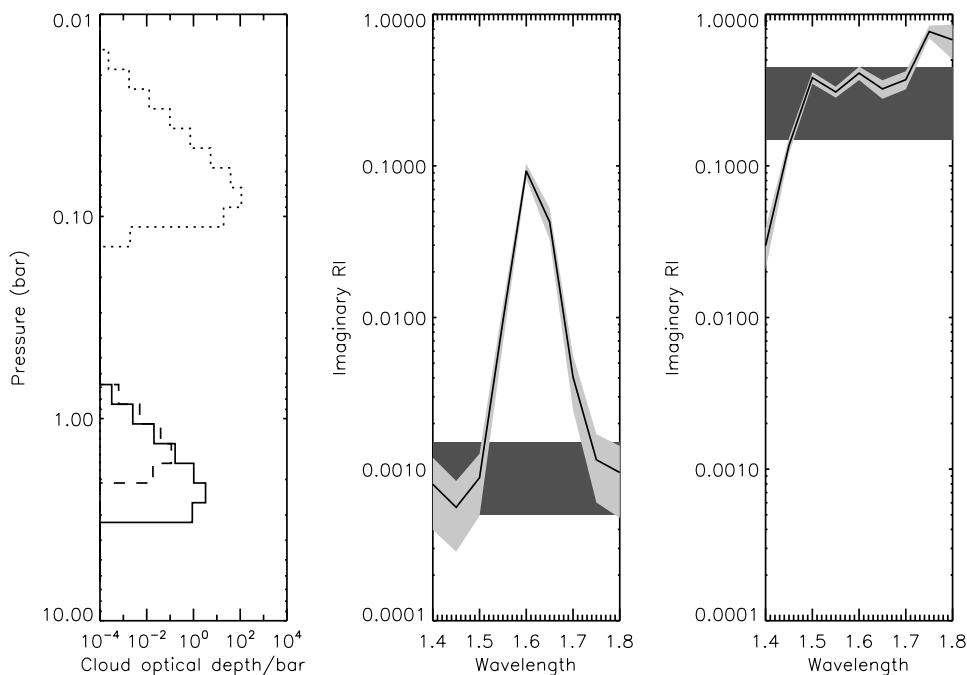
Fig. 16.— Retrieved cloud/haze opacity profile and imaginary refractive index spectra for the Tropospheric Cloud (TC) and Haze from the limb-scattering analysis in the latitude band $5 - 15°$S. As in Fig.11, the *a priori* value and range is indicated by the darker shaded region, while the retrieved spectra and errors are indicated with the solid line and lighter shaded region, respectively. The cloud/haze positions are well-constrained as are the imaginary refractive index spectra of both the TC and the Haze in this case. NB In these retrievals the *a priori* haze complex refractive index was set to $1.4 + 0.3i$ at all wavelengths, as described in the text, while the *a priori* tropospheric cloud complex refractive index was set again to $1.4 + 0.001i$.
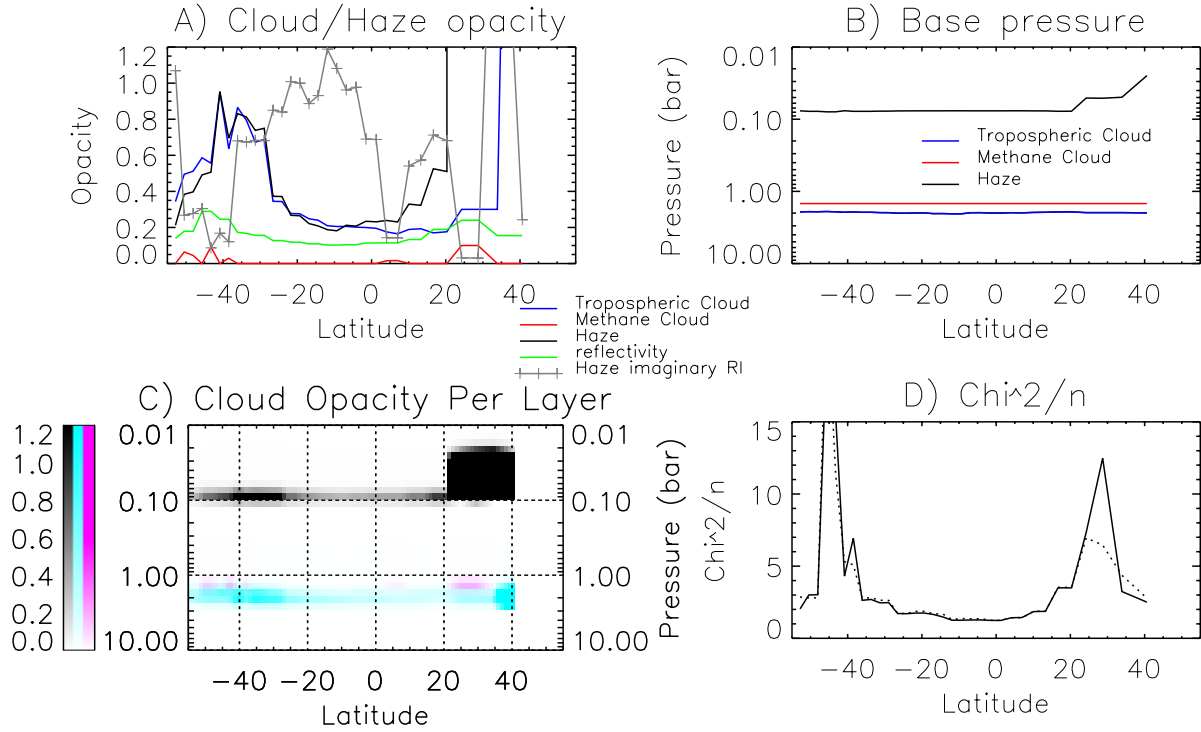
Fig. 17.— As Fig.13, but showing the retrieved cloud/haze opacities and base pressures as a function of latitude along the selected line for observation 'OB34' (Fig.9). Here the Haze particles are assumed to be less scattering with an *a priori* complex refractive index set to $1.4 + 0.3i$ at all wavelengths and allowed to vary. The tropospheric cloud particles have the same *a priori* complex refractive index of $1.4 + 0.001i$. Panel A additionally plots the retrieved imaginary refractive index of the Haze particles at 1.65 μm. As before, the χ^2/n for the two-cloud (solid line) and three-cloud (dotted line) models is shown in Panel D. NB the labels for Panel A have been moved to the centre for clarity.

Fig. 18.— As Fig.13, but showing retrieved cloud/haze opacities and base pressures as a function of latitude along the selected line for 'OB37', which runs through the 'intermediate-level' cloud at $\sim 10°$N, together with the estimated χ^2/n of the two-cloud (solid line) and three-cloud (dotted line) model fits. In these retrievals the *a priori* Haze complex refractive index was again set to $1.4 + 0.001i$ at all wavelengths and fixed, while the complex refractive index spectra of the tropospheric cloud particles was allowed to vary. A poor fit is obtained in the region of the near-equatorial 'intermediate-level' cloud for both models.
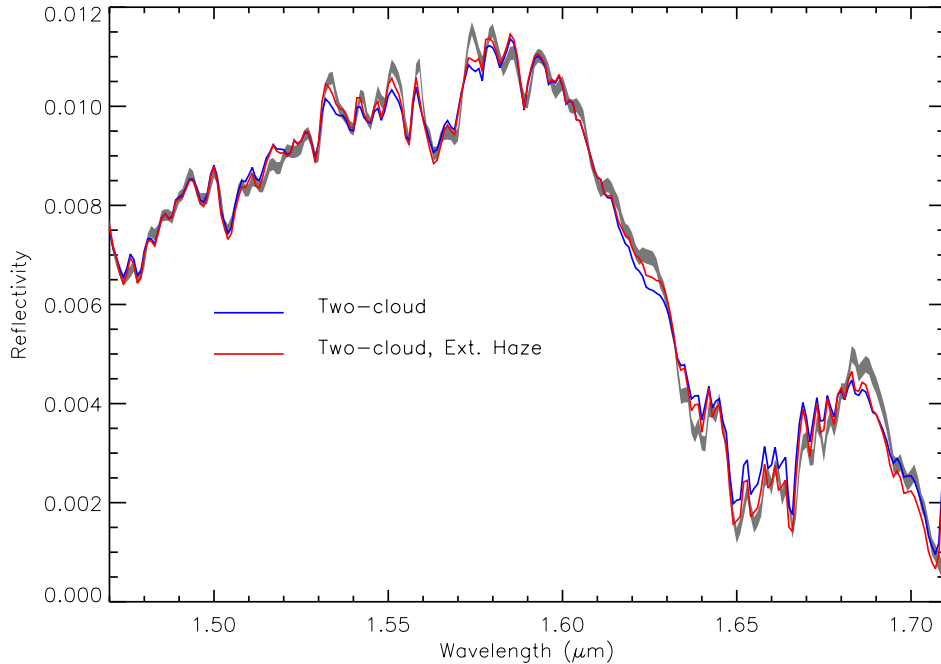
Fig. 19.— Retrieved spectrum for sample pixel at 10.7°S in the 'intermediate-level' cloud (indicated in panel (b) of Fig.9) where our fit is worst for the 'OB37' line sample. The form of the figure is identical to Fig. 10 and again the grey shaded region is the measured spectrum and errors. The fit with our original two-cloud model is shown in blue, while that in which the Haze is allowed to be vertically extended (i.e. not made to be physically thin), with an *a priori* fractional scale height of 0.5 ± 0.1 and with a higher *a priori* base pressure of 0.25 bar (compared with 0.08 bar before) is shown in red and can be seen to significantly improve the fit.
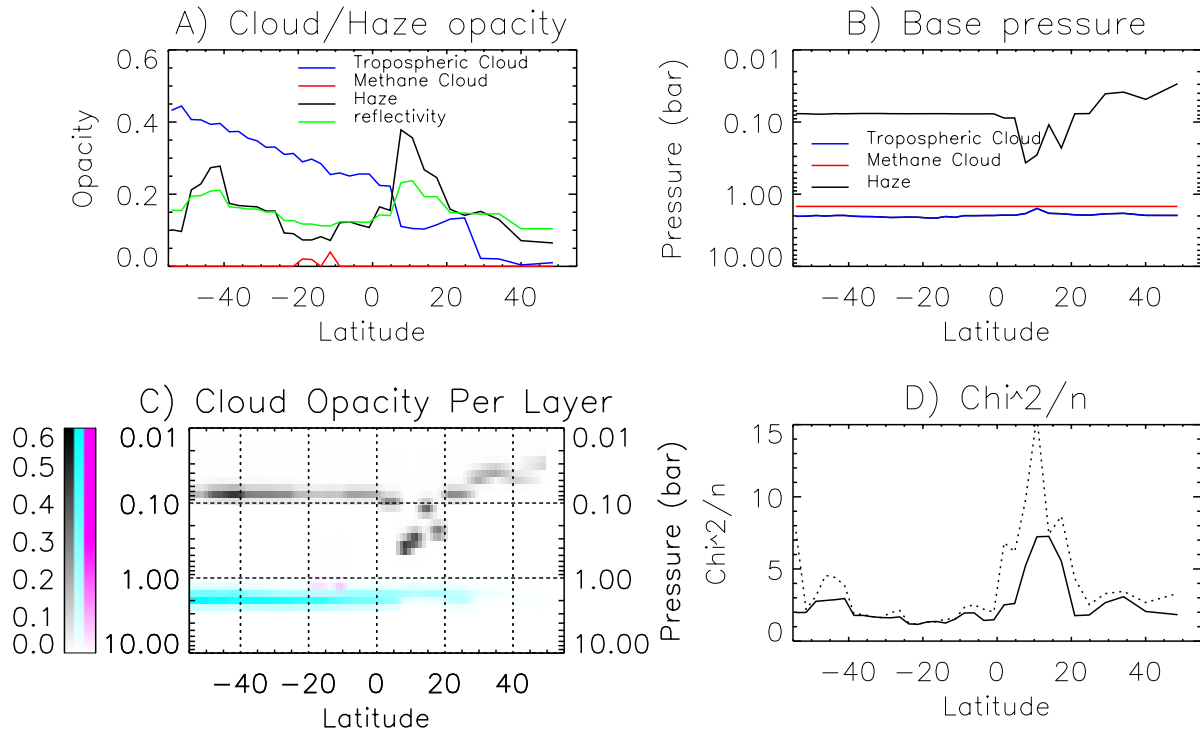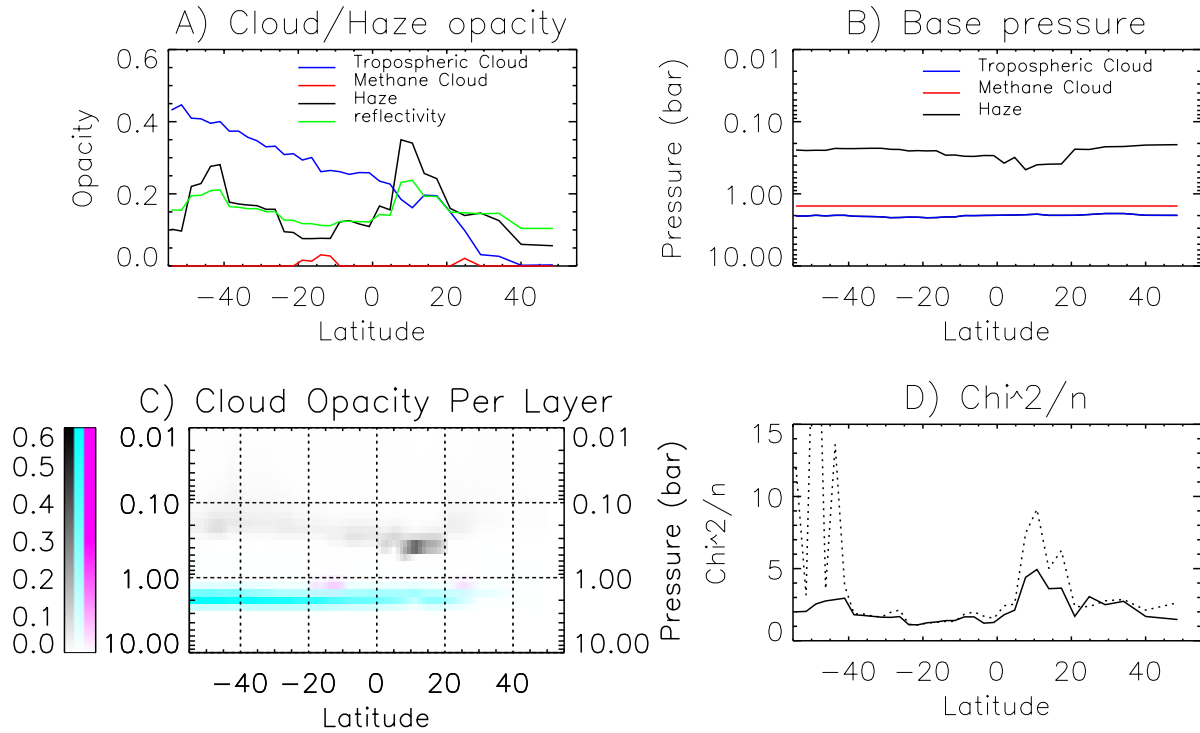
Fig. 20.— As Fig.18, but showing retrieved cloud/haze opacities and base pressures as a function of latitude along the selected line for 'OB37' where the Haze *a priori* base pressure was increased to 0.25 bar and the distribution allowed to be vertically extended with an *a priori* fractional scale height of 0.5 ± 0.1. The fit in the region of the 'intermediate-level' cloud can be seen to be significantly improved as compared with Fig.18.

Table 1.   2013 VLT Observations.

Name	Date	T_1[a]	T_2[a]	Grism	T_{exp}[a]	NDIT[a]	Plate Scale
OB1[b]	9th October 2013	23:52	23:55	H	180s	1	0.1″
OB2	10th October 2013	00:14	00:18	J	180s	1	0.1″
OB3[c]	10th October 2013	00:21	00:25	J	180s	1	0.1″
OB4	10th October 2013	00:28	00:32	J	180s	1	0.1″
OB5	10th October 2013	00:36	00:39	J	180s	1	0.1″
OB6	10th October 2013	00:46	00:49	H	180s	1	0.1″
OB7	10th October 2013	00:53	00:56	H	180s	1	0.1″
OB8	10th October 2013	01:00	01:04	H	180s	1	0.1″
OB9	10th October 2013	01:07	01:11	H	180s	1	0.1″
OB10	10th October 2013	01:15	01:19	H	180s	1	0.1″
OB11	10th October 2013	01:23	01:26	H	180s	1	0.1″
OB12	10th October 2013	01:30	01:34	H	180s	1	0.1″
OB13[b]	10th October 2013	04:24	04:28	H	180s	1	0.1″
OB14	10th October 2013	04:31	04:35	H	180s	1	0.1″
OB15	10th October 2013	04:38	04:42	H	180s	1	0.1″
OB16	10th October 2013	04:45	04:49	H	180s	1	0.1″
OB17	10th October 2013	04:53	04:56	H	180s	1	0.1″
OB18	10th October 2013	05:00	05:03	H	180s	1	0.1″
OB19	10th October 2013	05:10	05:14	J	180s	1	0.1″
OB20	10th October 2013	05:17	05:21	J	180s	1	0.1″
OB21	10th October 2013	05:24	05:28	J	180s	1	0.1″

Table 1—Continued

Name	Date	T_1[a]	T_2[a]	Grism	T_{exp}[a]	NDIT[a]	Plate Scale
OB22[c]	10th October 2013	05:32	05:35	J	180s	1	0.1″
OB23[c]	10th October 2013	05:40	05:43	J	180s	1	0.1″
OB24	11th October 2013	00:03	00:05	H	60s	1	0.1″
OB25	11th October 2013	00:08	00:10	J	60s	1	0.1″
OB26	11th October 2013	00:29	00:30	H	60s	1	0.1″
OB27[b]	11th October 2013	00:48	01:48	H	70s	2	0.025″
OB28	11th October 2013	03:20	03:22	H	60s	1	0.1″
OB29	11th October 2013	03:26	03:27	J	60s	1	0.1″
OB30[b]	11th October 2013	03:40	04:40	H	70s	2	0.025″
OB31	11th October 2013	04:40	04:42	H	60s	1	0.1″
OB32	11th October 2013	04:44	04:45	H	60s	1	0.1″
OB33	11th October 2013	04:50	04:51	J	60s	1	0.1″
OB34	12th October 2013	00:01	00:03	H	60s	1	0.1″
OB35	12th October 2013	00:08	00:10	J	60s	1	0.1″
OB36[b]	12th October 2013	00:30	01:25	H	70s	2	0.025″
OB37	12th October 2013	03:48	03:50	H	60s	1	0.1″
OB38	12th October 2013	03:55	03:56	J	60s	1	0.1″
OB39[b]	12th October 2013	04:08	05:02	H	70s	2	0.025″

[a]T_1 and T_2 are the start and end time (UT) of each observation (hh:mm), T_{exp} is the exposure time, NDIT is the number of exposures per observation.

[b]Data included in scan image in Fig. 5

[c]Poor image quality and not included in analysis

Table 2: Summary of Gemini-N/NIFS Neptune observations in the 2011 campaign.

Date	T_1	T_2	Grism	Integration Time
30th August 2011	10:35	11:28	I	20min (2min ×10 frames)
1st September 2011	09:44	10:38	H	20min (2min ×10 frames)
1st September 2011	10:49	11:54	J	20min (2min ×10 frames)[a]
5th September 2011	06:15	06:42	J	10min (2min ×5 frames)
6th September 2011	06:27	07:20	I	20min (2min ×10 frames)
6th September 2011	08:00	08:54	H	20min (2min ×10 frames)
7th September 2011	07:45	08:38	J	20min (2min ×10 frames)
9th September 2011	06:16	07:09	I	20min (2min ×10 frames)
11th September 2011	06:00	06:53	H	20min (2min ×10 frames)

[a]Not shown in Fig.8 as it overlaps on figure with previous observation.